Intercalation-conversion hybrid cathodes enabling Li–S full-cell architectures with jointly superior gravimetric and volumetric energy densities

Weijiang Xue [1], Zhe Shi[1], Liumin Suo [1,2,3,4]*, Chao Wang[1], Ziqiang Wang[1], Haozhe Wang [5], Kang Pyo So[1], Andrea Maurano [6], Daiwei Yu[5], Yuming Chen[1], Long Qie[1,7], Zhi Zhu[1], Guiyin Xu [1], Jing Kong[5] and Ju Li [1]*

A common practise in the research of Li–S batteries is to use high electrode porosity and excessive electrolytes to boost sulfur-specific capacity. Here we propose a class of dense intercalation-conversion hybrid cathodes by combining intercalation-type Mo_6S_8 with conversion-type sulfur to realize a Li–S full cell. The mechanically hard Mo_6S_8 with fast Li-ion transport ability, high electronic conductivity, active capacity contribution and high affinity for lithium polysulfides is shown to be an ideal backbone to immobilize the sulfur species and unlock their high gravimetric capacity. Cycling stability and rate capability are reported under realistic conditions of low carbon content (~10 wt%), low electrolyte/active material ratio (~1.2 µl mg^{-1}), low cathode porosity (~55 vol%) and high mass loading (>10 mg cm^{-2}). A pouch cell assembled based on the hybrid cathode and a 2× excess Li metal anode is able to simultaneously deliver a gravimetric energy density of 366 Wh kg^{-1} and a volumetric energy density of 581 Wh l^{-1}.

Anion-redox lithium–sulfur (Li–S) is one of the most promising conversion battery chemistries with high theoretical cathode energy density of 2,600 Wh kg^{-1} based on the weight of Li_2S, $S_8 + 16e^- + 16Li^+ = 8Li_2S$, several times higher than conventional lithium-ion battery (LIB) cathodes based on transition metal cation–redox intercalation reactions[1,2]. Unfortunately, the actual full-cell energy densities are a far cry from the theoretical values resulting from the excessive use of inactive components, such as electrolyte and conductive carbon. The electronic insulating nature of the S_8 and Li_2S phases (as compared to, say, Li_xCoO_2, with its high $Co^{3+} \leftrightarrow Co^{4+}$ polaron mobility) means that for the anion-redox reaction $S^{\alpha-} \leftrightarrow S^{\beta-} + (\alpha - \beta)e^-$ to proceed (where $0 \leq \alpha, \beta \leq 2$ is the average sulfur valence reflecting a mix of ionic and covalent bonding, often in the physical form of S_n^{2-}, where $\alpha = 2/n$), the S_8 must physically dissolve into liquid electrolytes as S_n^{2-} (electrolyte), transform into S_m^{2-} (electrolyte) and eventually redeposit somewhere else as solid phases.

This sulfur mobility is a key characteristic of many Li–S batteries, which has profound consequences on battery processes and performances. First, the dissolution of lithium polysulfide intermediates (LiPS) in the liquid electrolyte does help the kinetics. Even though LiPS is often written as Li_2S_n, one needs to understand that its solubilized form is $2Li^+$ (electrolyte) and S_n^{2-}(electrolyte), with individual solvation shells. A problem brought by such sulfur mobility is that S_n^{2-}(electrolyte) may physically cross over the separator to the Li metal anode in a non-blocking manner (so-called 'shuttling' of soluble redox mediators). This causes fast capacity fading on the

cathode side, even if we do not consider the ill effects this has on the anode[3]. Second, to enhance the sluggish redox kinetics of $S_8 \leftrightarrow Li_2S$, one needs a lot more liquid electrolyte and electrocatalytical surface areas in the cathode, which can be a common carbon black (which is neither a particularly good electrocatalyst, nor a good wetting substrate), or something more tailor made. Although a high fraction of conductive carbons (>30 wt%)[4] is usually required for sufficient sulfur use in conventional C/S_8 cathodes, it is equally true that such an excessive use (compared to LIB cathodes with 5 wt% carbon) of high-specific-area carbons gives rise to high cathode porosity (usually >70 vol%)[5], which demands a considerable amount of electrolyte to support a satisfactory ionic conductivity[6]. The theoretical prediction for the relationship between cathode porosity and cathode-specific energy densities in Fig. 1 shows that the porosity greatly affects both the cathode-specific gravimetric e_g and volumetric e_v energy densities. In most studies, a high electrolyte to active material ratio (E/AM ratio) >15 µl mg^{-1} (ref. [7])(~0.3 µl mg^{-1} for LIB cathode) is employed[8]. In other words, the most impressive high specific capacity based on just the S_8 weight is attained with a large excess of cathode porosity and electrolyte. In this case, the full-cell gravimetric E_g and volumetric E_v energy densities drop to an unacceptably low level. For example, with E/AM ratio >15 µl mg^{-1}, the full-cell E_g could not be higher than 175 Wh kg^{-1} even if reaching perfect sulfur utilization of 1,675 mAh g^{-1} (Supplementary Fig. 1). Another key challenge, becoming increasingly known[9,10] to make Li–S batteries less interesting for important markets, is the low E_v that is a crucial factor for many applications. The E_v evaluated from

[1]Department of Nuclear Science and Engineering and Department of Materials Science and Engineering, Massachusetts Institute of Technology, Cambridge, MA, USA. [2]Beijing Advanced Innovation Center for Materials Genome Engineering, Key Laboratory for Renewable Energy, Beijing Key Laboratory for New Energy Materials and Devices, Beijing National Laboratory for Condensed Matter Physics, Institute of Physics, Chinese Academy of Sciences, Beijing, China. [3]Center of Materials Science and Optoelectronics Engineering, University of Chinese Academy of Sciences, Beijing, China. [4]Songshan Lake Materials Laboratory, Dongguan, Guangdong, China. [5]Department of Electrical Engineering and Computer Science, Massachusetts Institute of Technology, Cambridge, MA, USA. [6]Advanced Materials Lab , Samsung Advanced Institute of Technology America, Burlington, MA, USA. [7]Institute of New Energy for Vehicles, School of Materials Science and Engineering, Tongji University, Shanghai, China. *e-mail: suoliumin@iphy.ac.cn; liju@mit.edu
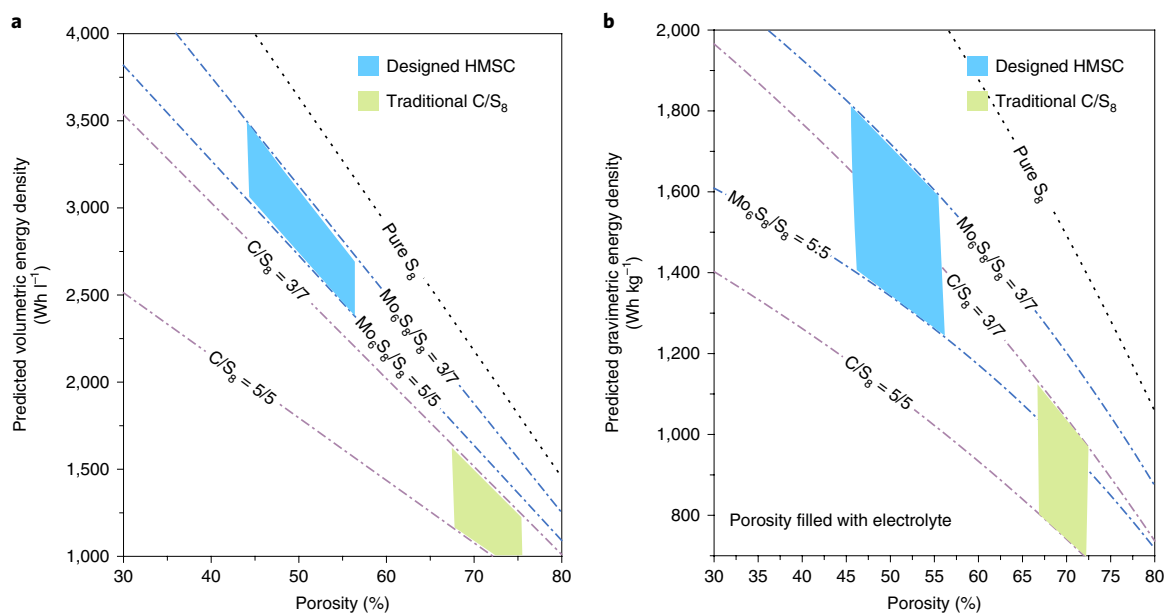
Fig. 1 | Design strategy for jointly high gravimetric–volumetric energy density. a,b, The relationship between cathode porosity and predicted cathode-specific e_v (**a**) and e_g (**b**) of the hybrid Mo_6S_8/S_8 cathode with all carbon included (hereafter referred to as HMSC) and C/S_8 cathode with different C/S_8 and Mo_6S_8/S_8 ratios. We correlate the required electrolyte amount to porosity by assuming that the electrolyte fills all the porosity in the cathode. Our intercalation-conversion strategy in principle would enable much higher e_g and e_v than conventional C/S_8 cathodes by reducing the cathode porosity from ~70 to 55 vol%. The calculation process is shown in Supplementary Note 1.

most studies[5] may be only ~400 Wh l^{-1}, lower than the conventional LiFePO$_4$|graphite battery (~500 Wh l^{-1})[11].

Great progress has been made on various structured sulfur cathodes to ameliorate the LiPS shuttling effect including sulfur-metal oxides or chalcogenide composites, for example, SiO_2 (refs. [12,13]), TiO_2 (refs. [14,15]), MnO_2 (refs. [16–18]), TiS_2 (refs. [19,20]) and VS_2 (ref. [21]). However, to reach high full-cell E_g and E_v, which is much more meaningful for pushing Li–S batteries into commercial development[22,23], Li–S batteries must work under rigorous conditions including high active material loading, lean electrolyte and low cathode porosity. Until now, however, few reports have been devoted to improving the joint E_g–E_v energy densities by decreasing the inactive components in sulfur cathodes. Nazar's group[4] developed a compact sulfur cathode using an in situ cross-linked elastomeric binder and successfully achieved a very low E/AM ratio of 3.5 μl mg^{-1}. A PEO-based polymer developed by Liu's group[8] acting as both Li$^+$ conducting binder and LiPS reservoir can further decrease the E/AM ratio to 3.3 μl mg^{-1}. Smart design of the electrolyte[24] and the pore structure of hosts[25] has been reported to improve the performances of Li–S batteries under lean electrolyte conditions. In addition, three-dimensional free-standing electrode architecture has also shown the potential of a compact electrode under low E/AM ratio conditions[26–28]. However, most of the reported sulfur cathodes cannot outperform the commercial LIB in terms of the joint E_g–E_v. To surpass today's LIB, it is essential to greatly diminish the inactive components, but it has been extremely challenging to achieve both high E_g and E_v by reducing cathode porosity and E/AM ratio simultaneously while maintaining acceptable rate capability.

To overcome this challenge, our strategy is to design an intercalation-conversion hybrid cathode material by introducing electrochemically active Chevrel-phase Mo_6S_8 with fast lithium intercalation reactions and high tap density to hybridize with S_8 (the HMSC material, Fig. 2a). The electronically conducting and electrochemically active Mo_6S_8 can effectively decrease the usage of high-surface-area carbons due to its extremely low electrical resistance (0.102 Ω sq^{-1} by a four-point probe method), reducing

cathode porosity from ~70 to 55 vol%. Such a hybrid design would, in principle, enable much higher E_g and E_v than traditional C/S_8 cathodes. The Chevrel-phase Mo_6S_8 has several unique properties. First, unlike most previous inactive materials employed in cathodes[13,14,29–39], it is able to contribute its own capacity in an ether-based electrolyte within the same voltage window as S_8 (1.7–2.8 V): $4Li^+ + 4e^- + Mo_6S_8 \leftrightarrow Li_4Mo_6S_8$. Second, this reaction is intercalative, and therefore has fast kinetics since $Li_xMo_6S_8$ has a high polaron mobility ($Mo^{2+} \leftrightarrow Mo^{3+}$). Third, because the theoretical density of Mo_6S_8 (5.04 g cm^{-3}) is much higher than that of S_8 (2.07 g cm^{-3}), the volumetric energy density of Mo_6S_8 is actually very respectable, 1,400 Wh l^{-1}, with an intrinsic rate capability comparable to LiFePO$_4$. Fourth, the affinity for LiPS can be greatly enhanced via in situ electrochemical lithiation of Mo_6S_8 to form $Li_xMo_6S_8$, thereby suppressing the shuttling effect and resulting in stable cyclability. Fifth, we also find that the Mo_6S_8 component improves the rheological properties of the slurry: the HMSC slurry has similar flow characteristics to the LIB slurry when coated on the current collector, it can be hard-pressed and is less prone to cracking, allowing us to easily reach high loadings such as 6.2 mg cm^{-2} for S_8 and 6.1 mg cm^{-2} for Mo_6S_8. Sixth and finally, after drying, even with much reduced porosity, the electrolyte wets the cathode easily. The mechanically hard Mo_6S_8 with fast Li$^+$ transport and nearly zero volume change during charge-discharge, is an ideal backbone to immobilize soft sulfur species and unlock their high gravimetric capacity. This material combination of Mo_6S_8 and S_8 is akin to the relation between the primer and the TNT in explosives, with one igniting quickly and another having high gravimetric energy density.

We would also like to add that the HMSC containing only ~10 wt% carbon (similar to a typical LIB cathode) shows good rate capability to 6 mA cm^{-2} and stable long-term cycling performance. More importantly, the cathode porosity is tremendously reduced and an extremely low E/AM ratio of 1.2 μl mg^{-1} can be realized. In particular, we can successfully make Ah-level pouch cells delivering high joint E_g and E_v of 366 Wh kg^{-1} and 581 Wh l^{-1}, outperforming both the Li–S and the commercial LIB in joint energy densities.
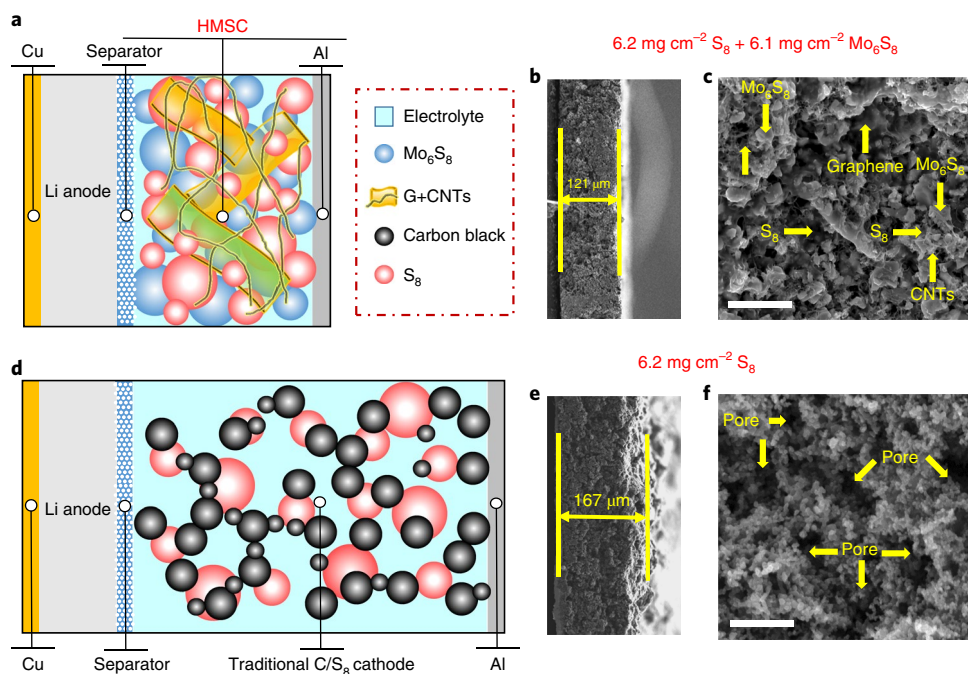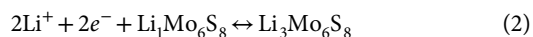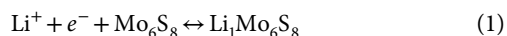
Fig. 2 | Characterizations of the HMSC and traditional C/S$_8$ cathode. a–f, Illustration of the Li–S batteries with our HMSC (**a–c**) and the C/S$_8$ cathode (**d–f**). SEM images show their cross-sections (**b,e**) and surfaces (**c,f**). The HMSC contains 6.2 mg cm^{-2} S$_8$ and 6.1 mg cm^{-2} Mo$_6$S$_8$ while the C/S$_8$ cathode contains only 6.2 mg cm^{-2} S$_8$. Compared with the C/S$_8$ cathode, our HMSC has much lower electrode porosity and packing density. Scale bars, 1 μm.

Fabrication and characterization of the HMSC cathode

Chevrel-phase Mo$_6$S$_8$ is a unique class of compounds that can accommodate both multivalent and monovalent cations[40]. Due to its unique open and stable structure, the Mo$_6$S$_8$ Chevrel phase features fast ion transport and good structural stability during lithiation/delithiation with a theoretical specific capacity of 128 mAh g^{-1} (refs. [41,42]). Although Mo$_6$S$_8$ has received attention as cathode/anode materials for Mg batteries[43] and aqueous Li-ion batteries[41], it has not been applied in Li–S batteries. In the operating voltage window of Li–S batteries from 1.7 to 2.8 V, the stoichiometry of Li insertion into Mo$_6$S$_8$ involves three stages[40],

$$Li^+ + e^- + Mo_6S_8 \leftrightarrow Li_1Mo_6S_8 \tag{1}$$

$$2Li^+ + 2e^- + Li_1Mo_6S_8 \leftrightarrow Li_3Mo_6S_8 \tag{2}$$

$$Li^+ + e^- + Li_3Mo_6S_8 \leftrightarrow Li_4Mo_6S_8 \tag{3}$$

The cyclic voltammetry profile in Supplementary Fig. 2 shows three cathodic peaks and three anodic peaks corresponding to equations (1)–(3). The lack of obvious decay in peak intensities indicates excellent reversibility of Li$_x$Mo$_6$S$_8$ in the ether-based electrolyte. The scanning electron microscopy (SEM) micrograph in Supplementary Fig. 3a reveals the irregular-shaped particles ranging from several hundred nanometres to several micrometres. A representative high-resolution transmission electron microscopy (HRTEM) image in Supplementary Fig. 3b clearly shows lattice fringes with a spacing of 0.36 nm, corresponding to (003) plane of rhombohedral Mo$_6$S$_8$.

The synthesis procedure of the HMSC material is shown in Supplementary Fig. 4. Carbon nanotubes (CNTs), graphene and Mo$_6$S$_8$ were firstly ball-milled to obtain a uniform mixture (Supplementary Fig. 5), and then a wet method[15,18] was used to deposit solid sulfur. The HMSC cathode contains 10 wt% carbonaceous materials (CNT/graphene), 85 wt% active S$_8$ + Mo$_6$S$_8$ and

5 wt% binder. The X-ray diffraction (XRD) result (Supplementary Fig. 6) clearly indicates that the Mo$_6$S$_8$ and S$_8$ are the dominant components of HMSC. The SEM image in Fig. 2c reveals a dense and uniform cathode morphology where CNTs and graphene can support a good three-dimensionally interconnected conductive network. Due to its good electronic conductivity and high tap density, the uniformly dispersed Mo$_6$S$_8$ not only offers an electronic matrix as good as carbon but also greatly decreases the carbon content from ~30 wt% in traditional C/S$_8$ cathodes to ~10 wt%, as low as traditional LIB cathodes. In contrast, the C/S$_8$ cathode shows a very porous morphology due to the large carbon content (36 wt%, Fig. 2f). The replacement of low-tap-density inactive components by high-tap-density electrochemically active components brings in significant advantages, described as follows.

The packing density of active materials can be effectively increased (Fig. 2a,b). The electrode thickness with 6.2 mg cm^{-2} S$_8$ for the C/S$_8$ cathode is 167 μm (Fig. 2e). In contrast, our HMSC with 6.2 mg cm^{-2} S$_8$ plus another 6.1 mg cm^{-2} Mo$_6$S$_8$ is only 121 μm (Fig. 2b). According to the normalized electrode thickness per 1 mg cm^{-2} S$_8$ summarized from previous studies in Supplementary Fig. 7, the typical values in most plausible C/S$_8$ electrodes are below 500 g l^{-1} (only S$_8$). However, the overall packing density of active materials in the HMSC doubles to 1,047 g l^{-1}, including 526 g l^{-1} (S$_8$) plus 521 g l^{-1} (Mo$_6$S$_8$).

Furthermore, it is much easier for our HMSC to obtain crack-free electrodes with high sulfur loading, which is essential for practically viable batteries[44] than traditional C/S$_8$ cathodes. For C/S$_8$ cathodes with high fraction of carbonaceous materials to achieve successful casting, the slurry needs many solvents to be diluted to a proper viscosity. Large cracks and morphology inhomogeneities in the C/S$_8$ cathode are observed due to excessive shrinkage during drying, while the HMSC is smooth and free of cracks (Supplementary Fig. 8). Benefiting from this approach, we can obtain a crack-free and highly compact electrode with very high loading of active materials (as high as 10 mg cm^{-2} S$_8$ and 9.9 mg cm^{-2} Mo$_6$S$_8$, Supplementary Fig. 9). When coated on current collector, the slurry mechanically
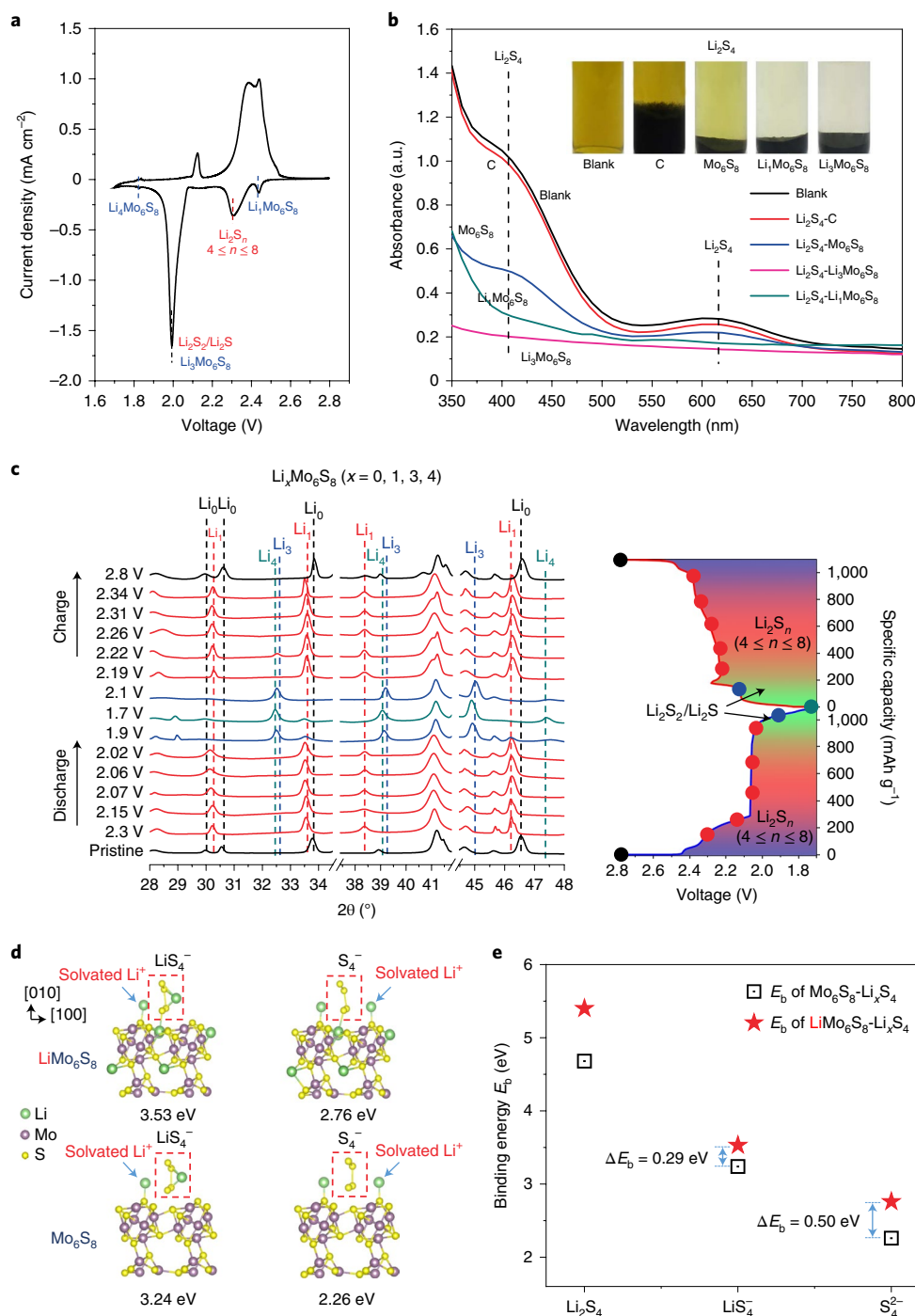
Fig. 3 | Investigation of the interaction between Li$_x$Mo$_6$S$_8$ and LiPS. a, Cyclic voltammetry plot of a Li|HMSC cell. **b**, Visual discrimination (inset) and ultraviolet-visible spectra of the Li$_2$S$_4$ solutions after exposure to C, Mo$_6$S$_8$, Li$_1$Mo$_6$S$_8$, Li$_3$Mo$_6$S$_8$ and Li$_4$Mo$_6$S$_8$. **c**, In situ XRD measurements of a Li|HMSC cell. **d**, Relaxed structures of LiS$_4^-$ and S$_4^{2-}$ after the respective step-wise ionization on their absorption on the Mo$_6$S$_8$ (100) and LiMo$_6$S$_8$ (100) surfaces, determined from density functional theory calculations. **e**, Comparison of different binding energies (E_b) between LiPS and Mo$_6$S$_8$/LiMo$_6$S$_8$ before and after the step-wise ionization.

feels like traditional LIB cathode slurry, and not like the typical C/S$_8$ slurry, due to the presence of hard Mo$_6$S$_8$ articles as dispersants. It can be hard-pressed like a LIB cathode, unlike a typical C/S$_8$ cathode.

Enhanced interaction between Li$_x$Mo$_6$S$_8$ and LiPS

Unlike conventional inactive host materials with a fixed affinity for LiPS, the chemical composition of Li$_x$Mo$_6$S$_8$ undergoes continuous variation during the charge-discharge processes, thus presenting a different chemical adsorption to LiPS with the voltage change. The

cyclic voltammetry characteristics measured on an HMSC|PP|Li half-cell in Fig. 3a clearly point to multiple redox reactions during the charge-discharge process and the highly reversible nature of the electrode. The representative cathodic peak at 2.43 V can be attributed to the lithiation of Mo$_6$S$_8$ to Li$_1$Mo$_6$S$_8$. The two representative cathodic peaks at roughly 2.3 and 2.0 V are attributed to the lithiation of S$_8$ to soluble LiPS (Li$_2$S$_n$, $4 \leq n \leq 8$) and insoluble short-chain Li$_2$S$_2$/Li$_2$S, respectively. The unrecognized cathodic peaks of Li$_3$Mo$_6$S$_8$ and Li$_4$Mo$_6$S$_8$ may result from the overlap with redox
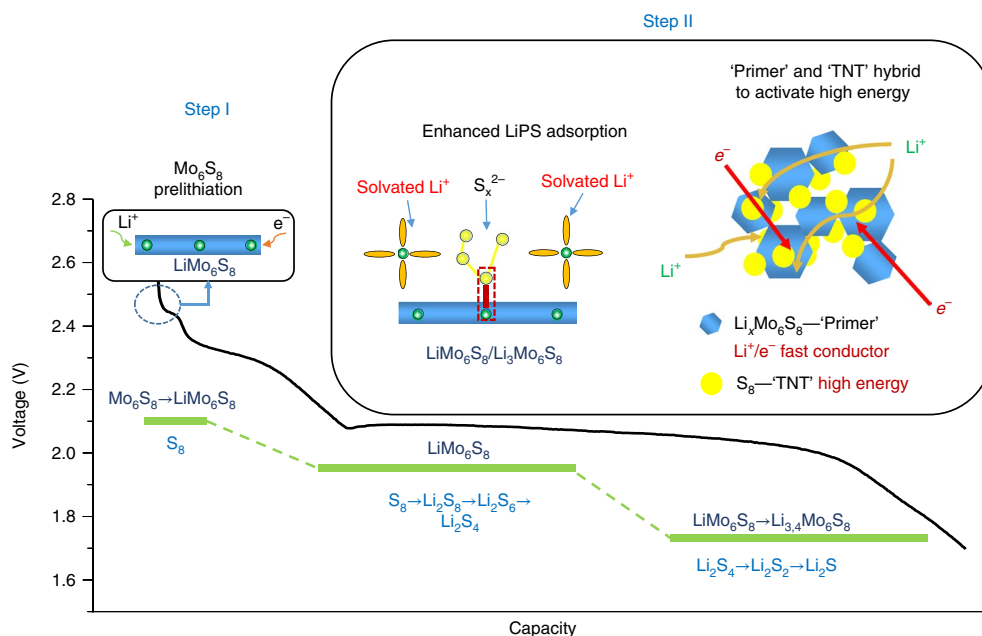
Fig. 4 | The roles of the Chevrel-phase Mo_6S_8 in the HMSC. Step I is a pre-lithiation step, proceeding before the reduction of sulfur (>2.4 V). Step II is the post-lithiation step, in which the lithiated Mo_6S_8 induces two functions. First, the interaction between LiPS and $LiMo_6S_8/Li_3Mo_6S_8$ is enhanced by the formation of the bonding between Li and S that dominates the adsorptive interaction. Second, the intercalative reaction in $Li_xMo_6S_8$ provides a fast Li-ion transport channel that can unlock the gravimetric capacity of S_8.

peaks of S_8. To gain an insight into the phase evolution of $Li_xMo_6S_8$, we conducted in situ XRD analysis during the charge-discharge process (Fig. 3c). In the initial stage, the pristine sample contains only rhombohedral Mo_6S_8. It is noted that no obvious peak associated with S_8 can be identified because of its much lower intensity compared to Mo_6S_8. When the cell is initially discharged to 2.3 V, three characteristic peaks located at 30.7, 33.9 and 46.7° shift towards lower angles indicating an increase in the lattice constants after Li intercalation, corresponding to rhombohedral $Li_1Mo_6S_8$ (JCPDS: 081–0858). Discharging further from 2.3 to 2.0 V, rhombohedral $Li_1Mo_6S_8$ is the dominant phase accompanying the continuous reduction of S_8 to soluble high-order LiPS (Li_2S_n, $4 \leq n \leq 8$) and partially insoluble low-order Li_2S_2/Li_2S. When the cell is further discharged to 1.9 and 1.7 V, the characteristic peaks continue to shift to lower angles indicating the emergence of $Li_3Mo_6S_8$ (JCPDS: 81–0859) and $Li_4Mo_6S_8$ (JCPDS: 81–0860) corresponding to the full conversion from LiPS to solid Li_2S. During charging, all the phase evolution is reversible.

These results reveal that the transition from S_8 to LiPS occurs along with the transformation of $Li_1Mo_6S_8$ to $Li_3Mo_6S_8$, suggesting that the $Li_1Mo_6S_8/Li_3Mo_6S_8$ dominates the adsorption of LiPS. To further observe such interactions, the polysulfide adsorption experiment (Fig. 3b, inset) is designed by the visual discrimination of the colour changes of the Li_2S_4 solution with the same amount of adsorbent materials (C, Mo_6S_8, $Li_1Mo_6S_8$, $Li_3Mo_6S_8$). The intrinsic ability of Mo_6S_8 to adsorb Li_2S_4 reveals the strong interaction between metal sulfide surface and LiPS[1,35], whereas the carbon-Li_2S_4 solution remains almost the same as the blank Li_2S_4, indicative of weak surface interaction (and consequently unimpressive electrocatalytic activity). However, it is intriguing to note that the $Li_1Mo_6S_8$ and $Li_3Mo_6S_8$ show almost transparent solutions after exposure to LiPS. Such strong adsorption capability can be further verified by ex situ ultraviolet-visible spectroscopy measurements. Figure 3b clearly demonstrates the much higher absorbance of $Li_1Mo_6S_8$-Li_2S_4 and $Li_3Mo_6S_8$-Li_2S_4 solutions than Mo_6S_8-Li_2S_4 in the characteristic adsorption regions of Li_2S_4 at ~410 and 615 nm[45]. Furthermore, the well-matched S and Mo distribution in the cycled HMSC

(Supplementary Fig. 10) further indicates the excellent adsorption capability of $Li_xMo_6S_8$ with LiPS.

To address the fundamental mechanism of such enhanced affinity for LiPS, first-principles calculations were performed. Most of the previous modelling studies constructed oversimplified molecule-on-slab adsorption configurations. Without taking the LiPS dissolution in electrolyte into account, it would probably result in overestimating the binding energies. In fact, the solvation plays a very important role of triggering the ionization of LiPS into solvated Li^+ (electrolyte) cations and S_n^{2-} (electrolyte) anion (Fig. 3d). Therefore, the actual structure of LiPS in electrolytes could be LiS_n^-/S_n^{2-} and solvated Li^+. Herein, Li_2S_4 is employed as the representative LiPS. Figure 3d illustrates the adsorption configurations for LiS_4^- and S_4^{2-} on Mo_6S_8 and $LiMo_6S_8$ surfaces, respectively. The adsorptive interaction is dominated by the bonding between Li and S. Therefore, during the step-wise ionization of Li_2S_4 its binding strength with the substrate tends to drop with fewer Li atoms in Li_2S_4. However, compared to pristine Mo_6S_8, the $LiMo_6S_8$ with additional bond demonstrates a better anchoring capability that is reflected not only by the higher binding energy but also the smaller decrease in binding energy during the step-wise ionization (Fig. 3e). In the ether-based electrolyte, the interaction between the Li cation and polysulfide anion weakens with the increase of polysulfide chain length[46] and, consequently, there is an obvious decrement in the anchoring capability of the substrates, especially for those mainly via polar–polar Li–S interaction[7]. We propose from the simulation results that the prelithiated substrate has the advantage of stronger LiPS adsorption capability over the unlithiated one in the real LiPS-electrolyte system via the additional Li–S binding.

We propose a two-step role of Chevrel-phase Mo_6S_8 in Fig. 4. Step I is the pre-lithiation step (>2.4 V). During this step, Mo_6S_8 is transformed to $Li_xMo_6S_8$ ($x = 1$) before the reduction of sulfur. Subsequently, the $Li_xMo_6S_8$ exhibits two unique functions in Step II—the post-lithiation step. One is the enhanced LiPS adsorption: long-chain LiPS forms in the presence of $LiMo_6S_8$, benefiting the suppression of the shuttling effect and thus improving the cycling stability. Another is that the intercalative reaction in $Li_xMo_6S_8$
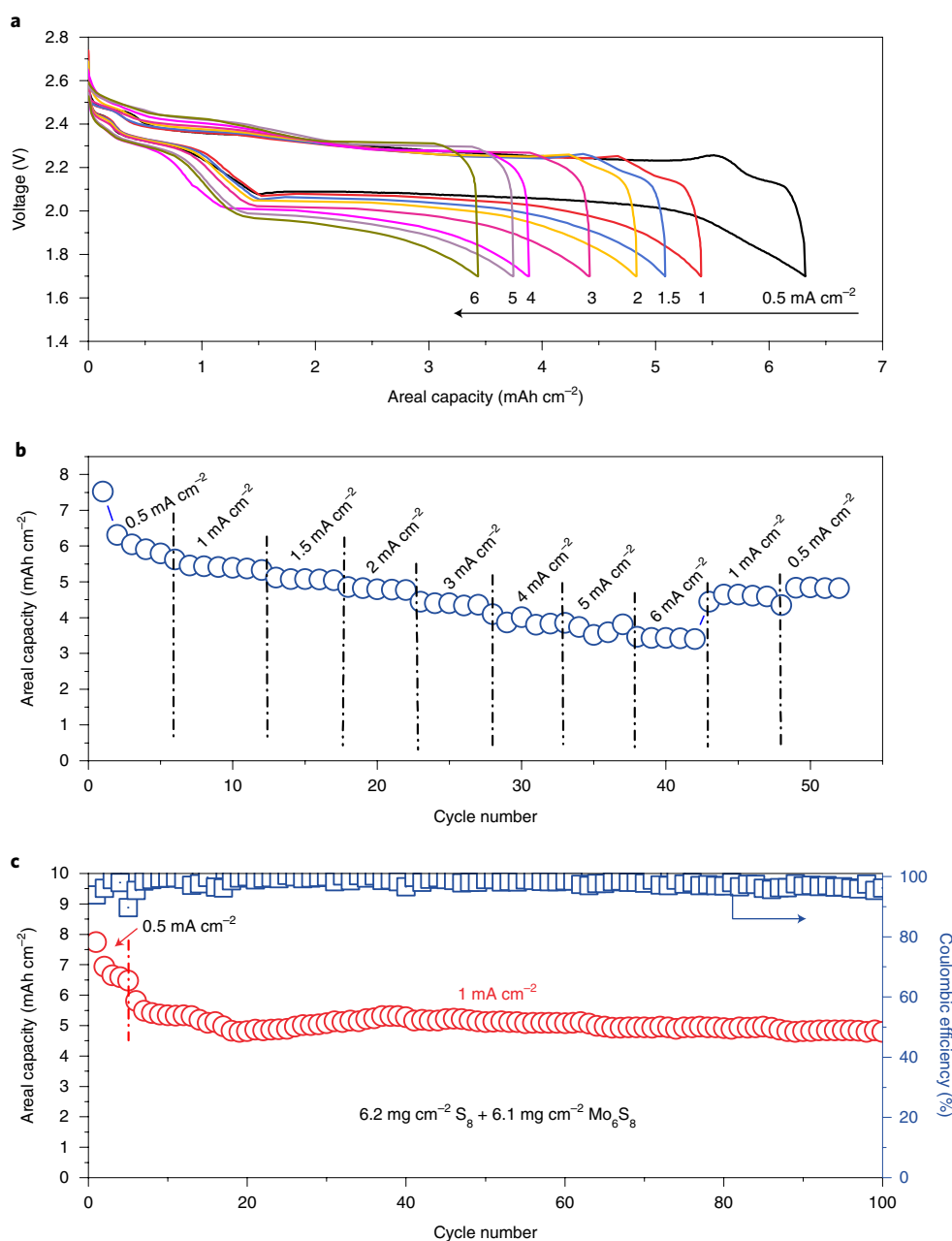
Fig. 5 | Electrochemical performance of the Li|HMSC coin cell. In this coin cell, we use: 6.2 mg cm⁻² S₈, 6.1 mg cm⁻² Mo₆S₈ and an E/AM ratio of 2.4 µl mg⁻¹. **a,b,** The charge-discharge profiles (**a**) and rate capability (**b**) at various current densities from 0.5 mA cm⁻² to 6 mA cm⁻². **c,** Cycling life and Coulombic efficiency at 1 mA cm⁻².

could provide a fast Li⁺ transporting channel, which is critical for unlocking the high gravimetric capacity of S_8.

Electrochemical performances

Despite the attractive high theoretical energy densities of a Li–S battery, it becomes increasingly clear that to achieve high full-cell E_g or E_v, improving the capacity at high sulfur loadings and keeping decent rate capability while decreasing the E/AM ratio and cathode porosity, is tremendously challenging[26,28,44,47]. To reach an E_g value roughly equal to 400 Wh kg⁻¹ or higher, it was suggested[48,49] that the E/AM ratio should be below 3 µl mg⁻¹ or even 1.9 µl mg⁻¹, and the cathode porosity must also be reduced as much as possible to achieve high E_v[5]. However, for standard C/S₈ cathodes, both high E/AM ratio and cathode porosity are required due to kinetics requirements.

The role of E/AM in attaining good electrochemical performance for C/S₈ is shown in Supplementary Fig. 11. At E/AM = 6 µl mg⁻¹, the areal capacity of the C/S₈ cathode reached about 5 mAh cm⁻² at 1 mA cm⁻², which dropped to <1 mAh cm⁻² at 1 mA cm⁻² after decreasing the E/AM ratio to 5 µl mg⁻¹ due to the increased cell impedance[26]. The required E/AM ratio can be effectively reduced to 4 µl mg⁻¹ by introducing only 20 wt% Mo₆S₈ into the cathode (Supplementary Fig. 12). By using an equal weight fraction of Mo₆S₈ and S₈ (Supplementary Fig. 13) with only ~10 wt% carbon in the cathode, the E/AM ratio can be successfully reduced to 2.4 µl mg⁻¹. The voltage profiles in Fig. 5a show long and flat discharge plateaus at ~2.1 V and low overpotential even at high current densities, indicating good electronic/ionic conductivities in the HMSC. In addition, apparent charge-discharge plateaus from Mo₆S₈ ↔ Li₁Mo₆S₈

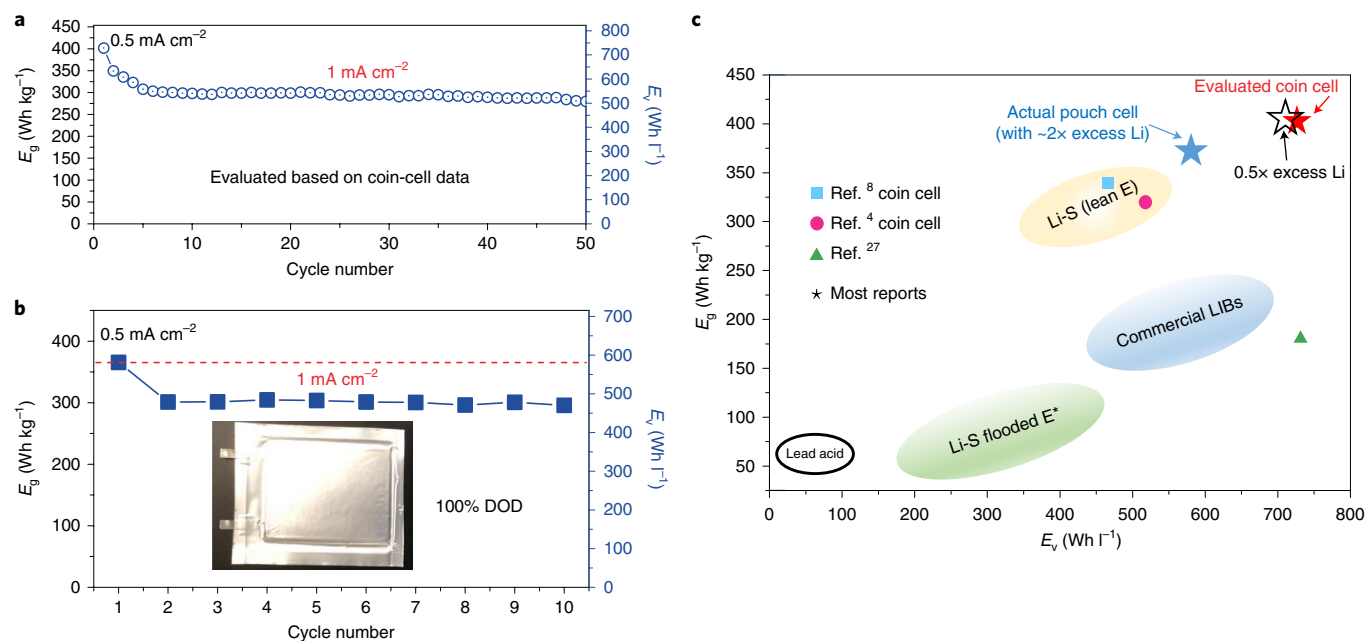**Fig. 6 | The E_g and E_v of the Li|HMSC cell. a**, The coin-cell configuration constructed by the HMSC cathode (6.9 mg cm^{-2} S$_8$ + 6.8 mg cm^{-2} Mo$_6$S$_8$) with an E/AM ratio ~1.5 µl mg^{-1} on cycling. **b**, The pouch-cell configuration constructed by the HMSC cathode with E/AM ratio ~1.2 µl mg^{-1} and ~2× Li excess (100 µm for one side). DOD, depth of discharge. **c**, The comparison of projected full-cell energy densities based on our data and representative publications. Reference [27] is evaluated on the basis of their pouch-cell data, and other references are based on coin-cell data.

at ~2.4 V can also be observed from Fig. 5a, further verifying that Mo$_6$S$_8$ indeed works with S$_8$ together as a secondary active material contributing an extra ~10% capacity (Supplementary Fig. 14). Our HMSC cathode exhibited excellent rate capability (Fig. 5b), achieving 7.5, 4.9, 4.0 and 3.5 mAh cm^{-2} at current densities of 0.5, 2, 4 and 6 mA cm^{-2}, respectively. The long-term cycling performance in Fig. 5c showed a high initial capacity of 7.8 mAh cm^{-2} with a good capacity retention of 83% over 100 cycles. Such good cycling stability could be attributed to the favourable LiPS adsorption capability of Li$_x$Mo$_6$S$_8$. In contrast, severe shuttling behaviour was found for the C/S$_8$ cathode without Mo$_6$S$_8$ (Supplementary Fig. 15). For such a high loading electrode and low E/AM, the rate capability and cycling stability are impressive.

Electrochemical impedance spectroscopy was conducted on HMSC cathode before and after cycling (Supplementary Fig. 16). The equivalent electrical circuit R$_0$ corresponded to the Ohmic resistance from the electrolyte solution. R$_1$/CPE$_1$ from the first semi-circle in the high-frequency range was assigned to the resistance of the surface layers on both cathode and anode. R$_2$/CPE$_2$ from the second semi-circle in the low-frequency range was attributed to the charge transfer process occurring at the interface between the cathode and electrolyte. R$_0$, R$_1$ and R$_2$ remained low and stable (Supplementary Fig. 17), indicating a favourable and well-maintained conducting network during cycling. The galvanostatic intermittent titration technique was also conducted to evaluate the state of health of the Li|HMSC battery after 100 cycles (Supplementary Fig. 18). In the voltage region between 2.1 and 2.5 V, small voltage changes on removing the current indicated relatively fast kinetics. Both the quasi-equilibrium potentials and the discharge plateau in the lower voltage region between 1.7 and 2.1 V remained stable and flat, suggesting a good state of health after 100 cycles. This is encouraging, since the cycle life of the Li|HMSC battery is not just controlled by the cathode, but also controlled by the Li metal anode that depletes the electrolyte[4] (Supplementary Fig. 19), which becomes more challenging under such lean electrolyte conditions.

For comparison of the full-cell energy densities of different Li–S works, we used a simplified pouch-cell model (Supplementary Fig. 20) to evaluate the coin-cell data, with 2× excess Li metal anode, cathode, electrolyte, Al current collector and separator all included. Our Li|HMSC cell with an E/AM ratio of ~1.5 µl mg^{-1} and low cathode porosity brought out extremely high joint E_g and E_v of 402 Wh kg^{-1} and 731 Wh l^{-1}, respectively, at 0.5 mA cm^{-2} and good cycling stability (Fig. 6a). The E_g is much higher than the commercial LIBs and the E_v is comparable to commercial LIBs. To the best of our knowledge, our full-cell joint E_g–E_v represents a very high level compared with most Li–S studies (Fig. 6c).

To validate the calculations above, 1 Ah-level pouch cells with multilayer cathodes (HMSC) and anodes (~2× excess Li metal[50], that is, 15-µm-thick Li metal opposite to every 1 mAh cm^{-2} HMSC), were assembled (Supplementary Fig. 21). The Li|HMSC pouch cell delivered energy densities of 366 Wh kg^{-1} and 581 Wh l^{-1} (Fig. 6b), comparable to our projected coin-cell data. The cycling of the Li|HMSC pouch cell was very stable. The voltage profiles (Supplementary Fig. 22) were identical to those of coin cells. The E/AM ratio in the pouch cell can be further reduced to a very lean electrolyte condition of 1.2 µl mg^{-1}, under which the pouch cell with traditional C/S$_8$ cathodes cannot even work (Supplementary Fig. 23). It is worth pointing out that there is still much room to further enhance the joint energy densities by optimizing both the mass-production process and other mechanical parameters for making the pouch cell, which is well-known to influence the practical performance[8]. For example, if 0.5× excess Li is used, we can further boost the energy densities to 405 Wh kg^{-1} and 712 Wh l^{-1} (Fig. 6c).

Conclusion

An intercalation-conversion composite cathode, created by hybridizing a mechanically hard Chevrel-phase Mo$_6$S$_8$ with fast lithium intercalation reactions and the mechanically soft S$_8$ with high gravimetric energy density, is reported in this paper. It has been shown to be an effective way to decrease the inactive components in Li–S battery cathodes, thus simultaneously achieving high E_g–E_v

and good rate capability. The Mo_6S_8 is an ideal backbone to immobilize soft sulfur species and unlock their high gravimetric capacity. The excellent areal capacity and cyclability at high active material loadings were enabled under realistic but challenging conditions including very low carbon content (~10 wt%), cathode porosity (~55 vol%) and E/AM ratio (1.2 μl mg^{-1}). To further demonstrate the practicality of our approach, we built Ah-level Li|HMSC pouch cells, which displayed very high joint energy densities of 366 Wh kg^{-1} and 581 Wh l^{-1} with quite abundant 2× excess lithium metal. This work overcomes the major limitations associated with pure anion-redox materials and will open new avenues for developing simultaneously high gravimetric and volumetric energy density batteries.

Methods

Preparation of Mo_6S_8. Chevrel-phase Mo_6S_8 was fabricated by a solid-state synthesis method. First, CuS (99% Sigma-Aldrich), Mo (99.99% Sigma-Aldrich) and MoS_2 (99% Sigma-Aldrich) were ground for 0.5 h, then the mixtures were pressed into a pellet by a 14-mm-diameter mould and sealed in Swagelok stainless steel tube, which was gradually heated to 900 °C for 24 h at 2 °C min^{-1} in argon. Subsequently, the as-received $Cu_2Mo_6S_8$ precursors were added into a 6 M HCl solution for 12 h with oxygen bubbling to leach out Cu. After the reaction, the obtained Mo_6S_8 powder was centrifuged and washed with deionized water three times followed by drying at 60 °C overnight under a vacuum.

Preparation of the HMSC material. Sulfur was synthesized by a wet-method on the basis of the reaction between $Na_2S_2O_3$ and H_2SO_4. First, CNTs, graphene (both from Dr Bunshi Fugetsu, The University of Tokyo) and Mo_6S_8 were ball-milled to obtain a uniform slurry into which $Na_2S_2O_3$ was dissolved. Subsequently, 0.5 M H_2SO_4 was slowly added into the CNTs/graphene/Mo_6S_8/$Na_2S_2O_3$ mixture and stirred at room temperature for 2 h. The HMSC material was obtained after the mixture was washed, centrifuged and then dried at 60 °C overnight.

LiPS adsorption study. Mo_6S_8 powders were pressed into 14-mm-diameter pellets. Then, CR2032-type coin cells were then assembled using Mo_6S_8 pellets as cathodes, Celgard separators and Li metal as anodes in the Ar-filled glove box. The electrolyte was 1 M lithium bis-(trifluoromethanesulfonyl) imide (LiTFSI) in a 1,3-dioxolane(DOL)-dimethoxyethane (DME) mixture (1:1, v/v) with 2 wt% LiNO$_3$. The cells were galvanostatically discharged to 2.3 and 1.9 V at a current density of 0.2 mA cm^{-2} using a Landt CT 2001A battery cycler to obtain electrochemical lithiated $Li_1Mo_6S_8$ and $Li_3Mo_6S_8$, respectively. Finally, the $Li_1Mo_6S_8$ and $Li_3Mo_6S_8$ products were collected by washing and drying the cathode materials after disassembling the coin cells in the glove box.

Li_2S_4 solutions were synthesized by reacting lithium sulfide (Li_2S) and elemental sulfur in the desired ratio in anhydrous DME solvent in an Ar-filled glove box. For the LiPS adsorption study, Mo_6S_8, $Li_1Mo_6S_8$, $Li_3Mo_6S_8$ were added to glass vials. Subsequently, Li_2S_4 solutions were added. Two blank vials were also filled with the same blank Li_2S_4 solution and the Li_2S_4-carbon black (Timical, Super C65) mixture as control samples, respectively. The adsorption ability of Mo_6S_8, $Li_1Mo_6S_8$, $Li_3Mo_6S_8$ and carbon on LiPS was qualitatively determined by using a ultraviolet-visible spectrometer (Perkin Elmer Lambda 1050 Spectrophotometer).

Characterization. The morphologies and microstructures were characterized by SEM (Zeiss Merlin high-resolution SEM) with energy-dispersive X-ray analysis and transmission electron microscopy (TEM, JOEL 2010F). The sulfur content was determined by thermogravimetric analyses (TG-DSC, SDT Q600) under nitrogen protection. In situ XRD was performed using a Rigaku Smartlab XRD system coupled with a specialized battery cell to monitor the phase evolution during the discharge and charge. The electronic conductivities were measured by a standard four-point-probe resistivity measurement system.

Electrochemical measurements. A slurry was fabricated by mixing 95 wt% of the HMSC and 2.5 wt% of styrene butadiene rubber aqueous binder, and 2.5 wt% of carboxymethyl cellulose binder. The obtained slurry was doctor-bladed onto a carbon-coated aluminum foil and then dried at 60 °C for 12 h. Finally, all the electrodes were rolled and cut into round discs. CR2032-type coin cells were assembled using the HMSC cathode and Li metal anode in the Ar-filled glove box. The electrolyte was 0.6 M LiTFSI in a DOL-DME mixture (1:1, v/v) with 0.4 M LiNO$_3$. E/AM ratio is calculated by the electrolyte volume over the active materials mass (in our case, Mo_6S_8 and S_8 are both considered active materials). For E/AM ratio of 1.5 μl mg^{-1}, Li metal was immersed into electrolyte for 12 h to form a passivation solid-electrolyte interphase layer before use. The cycling performances of the cells were measured by galvanostatic charge and discharge within the voltage window of 1.7–2.8 V versus Li/Li$^+$ at various current densities using a Landt CT 2001A battery cycler. Cyclic voltammetry and electrochemical impedance spectroscopy measurements were taken using an electrochemical workstation (Gamry Instruments, Reference 3000). The galvanostatic intermittent titration

technique was conducted on the cycled batteries that were subjected to current pulse intervals with a current density of 0.25 mA cm^{-2} for 10 min, followed by 10 min rests until complete discharge.

The evaluation of energy densities. On the basis of the simplified pouch-cell configuration shown in Supplementary Fig. 20, the jellyroll E_g and E_v can be evaluated the basis of coin-cell data using the equations

$$E_g = \frac{VC}{\sum m_i} \tag{4}$$

$$E_v = \frac{VC}{\sum T_i} \tag{5}$$

where E_g and E_v are the full-cell gravimetric (Wh kg^{-1}) and volumetric (Wh l^{-1}) energy densities, respectively, V is the average output voltage (2.1 V is assumed), C is the areal capacity (mAh cm^{-2}), m_i and T_i are the mass per unit square (mg cm^{-2}) and the thickness (cm) of cell components including the cathode, anode (2× Li excess is assumed), current collectors ($\rho_{Al} \approx 2.7$ g cm^{-3}), separator ($\rho \approx 0.95$ g cm^{-3}) and electrolyte ($\rho \approx 1.2$ g cm^{-3}). We do not take into account the electrolyte volume when calculating E_v. The jellyroll energy densities of pouch cells are calculated on the basis of actual measurements.

Pouch-cell assembly. First, the well-mixed slurry was double-side coated on carbon-coated Al foil and then dried at 60 °C for 4 h. Second, 4.3 × 5.6 cm^2 electrodes were cut by a gas driven die cutter (MTI Corporation) and the electrode materials were carefully removed from tab areas to expose the Al foil. The assembly process of a pouch cell is as follows. First, the Ni tab was pressed to attach with the Li foil and then was covered with 25-μm-thick Celgard separator. Second, the cathode and anode were carefully stacked layer-by-layer by hand to make a jellyroll cell. Third, the Al tab was welded together with cathodes. Finally, the jellyroll cell was vacuum-sealed by Al laminated films after injecting electrolyte.

First-principles calculations. We used the Perdew–Burke–Ernzerhof[51] exchange-correlational functional and the projector-augmented wave method[52] in our density functional theory (DFT) simulations implemented by the Vienna Ab Initio Simulation Package[53]. The DFT-Tkatchenko–Scheffler method[54] was used to take into account the van der Waals interactions in any adsorption processes. A plane wave basis set with an energy cutoff of 500 eV was adopted to expand the electronic wavefunctions. The Brillouin zone integration was conducted on a 5×5×1 Monkhorst–Pack k-point mesh. Atomic coordinates in all structures were relaxed until the maximum residual force below 0.02 eV Å^{-1}.

The Mo_6S_8 (001) surface has the lowest energy (24 meV Å^{-2}) and has been determined as the most stable surface among other low Miller index planes[55]. A slab of 1.5 Mo_6S_8 atomic layers (the bottom 0.5 layer frozen during optimization) was constructed to model the Mo_6S_8 (001) surface and a vacuum spacing larger than 10 Å was put on top of the slab to avoid interactions. The optimized bulk unit cell (Supplementary Fig. 24) has a lattice constant of 6.50 Å that matches the experimental value very well[56]. The optimized geometry of the configuration of the pristine Mo_6S_8 and the Li-intercalated Mo_6S_8 ($LiMo_6S_8$) is shown in Supplementary Fig. 25. To simulate the $Li_1Mo_6S_8$ in our experiment, Li atoms are intercalated into the spacious sites surrounded by four Mo_6S_8 clusters, which is in agreement with typical metallic ion intercalation in Chevrel-phase Mo_6S_8 determined by both experiment and computation[57].

The binding energy (E_b) is defined as the difference between the total energy of the Li_2S_4-adsorbed system (E_{total}), and the energy sum of isolated Li_2S_4 and a clean Mo_6S_8 surface (with or without Li intercalation):

$$E_b \equiv E_{Li_2S_4} + E_{surface} - E_{total} \tag{6}$$

A larger value indicates greater adsorbing ability.

Data availability

The data that support the plots in this paper and other findings of this study are available from the corresponding author on reasonable request.

References

1. Liu, X., Huang, J. Q., Zhang, Q. & Mai, L. Nanostructured metal oxides and sulfides for lithium-sulfur batteries. *Adv. Mater.* **29**, 1601759 (2017).
2. Manthiram, A., Fu, Y., Chung, S. H., Zu, C. & Su, Y. S. Rechargeable lithium-sulfur batteries. *Chem. Rev.* **114**, 11751–11787 (2014).
3. Zhang, S., Zhao, K., Zhu, T. & Li, J. Electrochemomechanical segradation of high-capacity battery electrode materials. *Prog. Mater. Sci.* **89**, 479–521 (2017).

4. Pang, Q., Liang, X., Kwok, C. Y., Kulisch, J. & Nazar, L. F. A comprehensive approach toward stable lithium-sulfur batteries with high volumetric energy density. *Adv. Energy Mater.* **7**, 1601630 (2016).
5. Xue, W. et al. Gravimetric and volumetric energy densities of lithium-sulfur batteries. *Curr. Opin. Electrochem.* **6**, 92–99 (2017).
6. Fan, F. Y. et al. Solvent effects on polysulfide redox kinetics and ionic conductivity in lithium-sulfur batteries. *J. Electrochem. Soc.* **163**, A3111–A3116 (2016).
7. Pang, Q., Liang, X., Kwok, C. Y. & Nazar, L. F. Advances in lithium–sulfur batteries based on multifunctional cathodes and electrolytes. *Nat. Energy* **1**, 16132 (2016).
8. Chen, J. et al. Improving lithium-sulfur battery performance under lean electrolyte through nanoscale confinement in soft swellable gels. *Nano Lett.* **17**, 3061–3067 (2017).
9. McCloskey, B. D. Attainable gravimetric and volumetric energy density of Li-S and Li-ion battery cells with solid separator-protected Li metal anodes. *J. Phys. Chem. Lett.* **6**, 4581–4588 (2015).
10. Choi, J. W. & Aurbach, D. Promise and reality of post-lithium-ion batteries with high energy densities. *Nat. Rev. Mater.* **1**, 16013 (2016).
11. Berg, E. J., Villevieille, C., Streich, D., Trabesinger, S. & Novák, P. Rechargeable batteries: grasping for the limits of chemistry. *J. Electrochem. Soc.* **162**, A2468–A2475 (2015).
12. Ji, X., Evers, S., Black, R. & Nazar, L. F. Stabilizing lithium–sulphur cathodes using polysulphide reservoirs. *Nat. Commun.* **2**, 325 (2011).
13. Xue, W. et al. Double-oxide sulfur host for advanced lithium-sulfur batteries. *Nano Energy* **38**, 12–18 (2017).
14. Tao, X. et al. Strong sulfur binding with conducting Magneli-phase $Ti_{(n)}O_{2(n-1)}$ nanomaterials for improving lithium-sulfur batteries. *Nano Lett.* **14**, 5288–5294 (2014).
15. Wei Seh, Z. et al. Sulphur-TiO_2 yolk-shell nanoarchitecture with internal void space for long-cycle lithium–sulphur batteries. *Nat. Commun.* **4**, 1331 (2013).
16. Liang, X. & Nazar, L. F. In situ reactive assembly of scalable core-shell sulfur-MnO_2 composite cathodes. *ACS Nano* **10**, 4192–4198 (2016).
17. Li, Z., Zhang, J. & Lou, X. W. Hollow carbon nanofibers filled with MnO_2 nanosheets as efficient sulfur hosts for lithium-sulfur batteries. *Angew. Chem. Int. Ed.* **54**, 12886–12890 (2015).
18. Liang, X. et al. A highly efficient polysulfide mediator for lithium–sulfur batteries. *Nat. Commun.* **6**, 5682 (2015).
19. Ma, L. et al. Hybrid cathode architectures for lithium batteries based on TiS_2 and sulfur. *J. Mater. Chem. A* **3**, 19857–19866 (2015).
20. Su, Y.-S. & Manthiram, A. Sulfur/lithium-insertion compound composite cathodes for Li-S batteries. *J. Power Sources* **270**, 101–105 (2014).
21. Zhou, G. et al. Catalytic oxidation of Li_2S on the surface of metal sulfides for Li-S batteries. *Proc. Natl Acad. Sci. USA* **114**, 840–845 (2017).
22. Lin, Z., Liu, T. F., P., A. X. & Liang, C. D. Aligning academia and industry for unified battery performance metrics. *Nat. Commun.* **9**, 5262 (2018).
23. Zhao, Q., Zheng, J. & Archer, L. Interphases in lithium-sulfur batteries: toward deployable devices with competitive energy density and stability. *ACS Energy Lett.* **3**, 2104–2113 (2018).
24. Pan, H. et al. Addressing passivation in lithium-sulfur battery under lean electrolyte condition. *Adv. Funct. Mater.* **28**, 1707234 (2018).
25. Wang, H. et al. Tailored reaction route by micropore confinement for Li-S batteries operating under lean electrolyte conditions. *Adv. Energy Mater.* **8**, 1800590 (2018).
26. Chung, S. H. & Manthiram, A. Rational design of statically and dynamically stable lithium-sulfur batteries with high sulfur loading and low electrolyte/sulfur ratio. *Adv. Mater.* **30**, 1705951 (2018).
27. Mao, Y. et al. Foldable interpenetrated metal-organic frameworks/carbon nanotubes thin film for lithium–sulfur batteries. *Nat. Commun.* **8**, 14628 (2017).
28. Chung, S.-H. & Manthiram, A. Designing lithium-sulfur cells with practically necessary parameters. *Joule* **2**, 710–724 (2018).
29. Bai, S., Liu, X., Zhu, K., Wu, S. & Zhou, H. Metal-organic framework-based separator for lithium–sulfur batteries. *Nat. Energy* **1**, 16094 (2016).
30. Xu, G. et al. Absorption mechanism of carbon-nanotube paper-titanium dioxide as a multifunctional barrier material for lithium-sulfur batteries. *Nano Res.* **8**, 3066–3074 (2015).
31. Wang, X. et al. Structural and chemical synergistic encapsulation of polysulfides enables ultralong-life lithium-sulfur batteries. *Energy Environ. Sci.* **9**, 2533–2538 (2016).
32. Peng, H. J. et al. Healing high-loading sulfur electrodes with unprecedented long cycling life: spatial heterogeneity control. *J. Am. Chem. Soc.* **139**, 8458 (2017).
33. Zhou, G. et al. A graphene foam electrode with high sulfur loading for flexible and high energy Li–S batteries. *Nano Energy* **11**, 356–365 (2015).
34. Zhang, Q. et al. Understanding the anchoring effect of two-dimensional layered materials for lithium-sulfur batteries. *Nano Lett.* **15**, 3780–3786 (2015).
35. Yuan, Z. et al. Powering lithium-sulfur battery performance by propelling polysulfide redox at sulfiphilic hosts. *Nano Lett.* **16**, 519–527 (2016).
36. Zang, J. et al. Hollow-in-hollow carbon spheres with hollow foam-like cores for lithium-sulfur batteries. *Nano Res.* **8**, 2663–2675 (2015).
37. Li, G. et al. Chemisorption of polysulfides through redox reactions with organic molecules for lithium–sulfur batteries. *Nat. Commun.* **9**, 705 (2018).
38. Pan, H. et al. Non-encapsulation approach for high-performance Li–S batteries through controlled nucleation and growth. *Nat. Energy* **2**, 813 (2017).
39. Tan, G. et al. Burning lithium in CS_2 for high-performing compact Li_2S-graphene nanocapsules for Li–S batteries. *Nat. Energy* **2**, 17090 (2017).
40. Levi, M. D. et al. Kinetic and thermodynamic studies of Mg^{2+} and Li^+ ion insertion into the Mo_6S_8 chevrel phase. *J. Electrochem. Soc.* **151**, A1044 (2004).
41. Suo, L. et al. 'Water-in-salt' electrolyte enables high-voltage aqueous lithium-ion chemistries. *Science* **350**, 938–943 (2015).
42. Mei, L. et al. Chevrel phase Mo_6T_8 (T = S, Se) as electrodes for advanced energy storage. *Small* **13**, 1701441 (2017).
43. Saha, P. et al. A convenient approach to Mo_6S_8 chevrel phase cathode for rechargeable magnesium battery. *J. Electrochem. Soc.* **161**, A593–A598 (2014).
44. Peng, H.-J., Huang, J.-Q., Cheng, X.-B. & Zhang, Q. Review on high-loading and high-energy lithium–sulfur batteries. *Adv. Energy Mater.* **7**, 1700260 (2017).
45. Cañas, N. A., Fronczek, D. N., Wagner, N., Latz, A. & Friedrich, K. A. Experimental and theoretical analysis of products and reaction intermediates of lithium-sulfur batteries. *J. Phys. Chem. C* **118**, 12106–12114 (2014).
46. Rajput, N. N. et al. Elucidating the solvation structure and dynamics of lithium polysulfides resulting from competitive salt and solvent interactions. *Chem. Mater.* **29**, 3375–3379 (2017).
47. Pope, M. A. & Aksay, I. A. Structural design of cathodes for Li-S batteries. *Adv. Energy Mater.* **5**, 1500124 (2015).
48. Hagen, M. et al. Lithium-sulfur cells: the gap between the state-of-the-art and the requirements for high energy battery cells. *Adv. Energy Mater.* **5**, 1401986 (2015).
49. Eroglu, D., Zavadil, K. R. & Gallagher, K. G. Critical link between materials chemistry and cell-level design for high energy density and low cost lithium-sulfur transportation battery. *J. Electrochem. Soc.* **162**, A982–A990 (2015).
50. Suo, L. et al. Fluorine-donating electrolytes enable highly reversible 5-V-class Li metal batteries. *Proc. Natl Acad. Sci. USA* **115**, 1156–1161 (2018).
51. Perdew, J. P., Burke, K. & Ernzerhof, M. Generalized gradient approximation made simple. *Phys. Rev. Lett.* **77**, 3865 (1996).
52. Blöchl, P. E. Projector augmented-wave method. *Phys. Rev. B* **50**, 17953 (1994).
53. Kresse, G. & Furthmüller, J. Efficient iterative schemes for ab initio total-energy calculations using a plane-wave basis set. *Phys. Rev. B* **54**, 11169 (1996).
54. Tkatchenko, A. & Scheffler, M. Accurate molecular van der Waals interactions from ground-state electron density and free-atom reference data. *Phys. Rev. Lett.* **102**, 073005 (2009).
55. Wan, L. F., Perdue, B. R., Apblett, C. A. & Prendergast, D. Mg desolvation and intercalation mechanism at the Mo_6S_8 Chevrel phase surface. *Chem. Mater.* **27**, 5932–5940 (2015).
56. Tarascon, J., DiSalvo, F., Murphy, D., Hull, G. & Waszczak, J. New superconducting ternary molybdenum chalcogenides in Mo_6Se_8, $T_1Mo_6S_8$, and $T_1Mo_6Se_8$. *Phys. Rev. B* **29**, 172 (1984).
57. Geng, L., Lv, G., Xing, X. & Guo, J. Reversible electrochemical intercalation of aluminum in Mo_6S_8. *Chem. Mater.* **27**, 4926–4929 (2015).

Acknowledgements

Author contributions

L.S., W.X. and J.L. conceived and designed the experiments. W.X., L.S. and C.W. fabricated the HMSC cathode. W.X., K.P.S., Y.C., L.Q., Z.Z. and G.X. carried out material characterization and electrochemical measurements. Z.S. carried out the DFT theoretical calculations. Z.W. and D.Y. carried out the TEM observation. H.W. and J.K. conducted the four-point-probe resistivity test. W.X., C.W. and A.M. made the pouch cell. W.X., L.S., J.L. and Z.S. wrote the paper. All authors discussed the results and reviewed the manuscript.

Competing interests

The authors declare no competing interests.

Additional information

Intercalation-conversion hybrid cathodes enabling Li–S full-cell architectures with jointly superior gravimetric and volumetric energy densities

Weijiang Xue [1], Zhe Shi[1], Liumin Suo [1,2,3,4]*, Chao Wang[1], Ziqiang Wang[1], Haozhe Wang [5], Kang Pyo So[1], Andrea Maurano [6], Daiwei Yu[5], Yuming Chen[1], Long Qie[1,7], Zhi Zhu[1], Guiyin Xu [1], Jing Kong[5] and Ju Li [1]*

[1]Department of Nuclear Science and Engineering and Department of Materials Science and Engineering, Massachusetts Institute of Technology, Cambridge, MA, USA. [2]Beijing Advanced Innovation Center for Materials Genome Engineering, Key Laboratory for Renewable Energy, Beijing Key Laboratory for New Energy Materials and Devices, Beijing National Laboratory for Condensed Matter Physics, Institute of Physics, Chinese Academy of Sciences, Beijing, China. [3]Center of Materials Science and Optoelectronics Engineering, University of Chinese Academy of Sciences, Beijing, China. [4]Songshan Lake Materials Laboratory, Dongguan, Guangdong, China. [5]Department of Electrical Engineering and Computer Science, Massachusetts Institute of Technology, Cambridge, MA, USA. [6]Advanced Materials Lab , Samsung Advanced Institute of Technology America, Burlington, MA, USA. [7]Institute of New Energy for Vehicles, School of Materials Science and Engineering, Tongji University, Shanghai, China. *e-mail: suoliumin@iphy.ac.cn; liju@mit.edu

Supplementary information
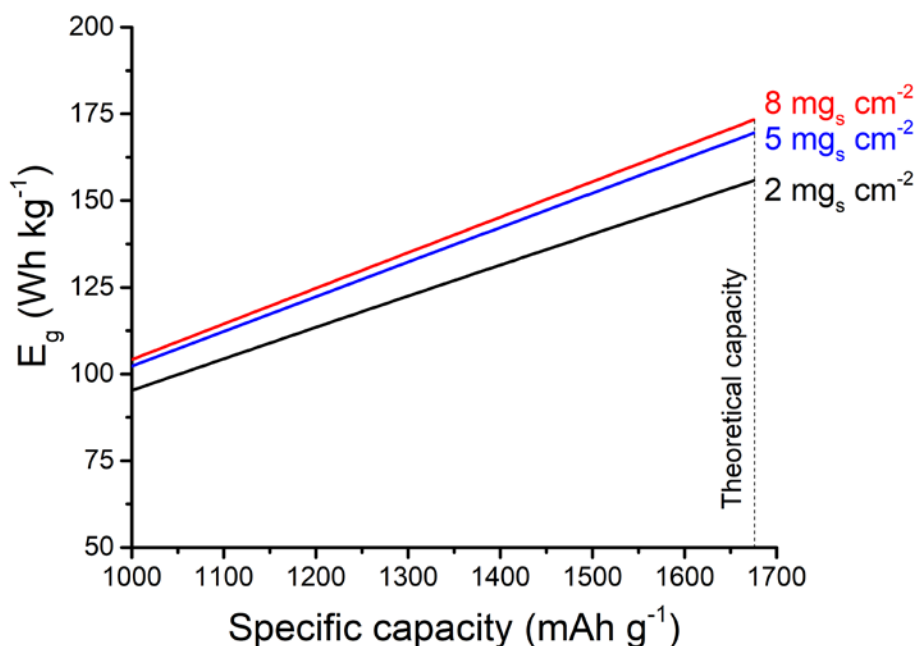
Supplementary Figure 1. The relationship between the estimated E_g and the specific capacity of sulfur under various sulfur loadings with E/AM ratio=15 µl mg^{-1} showing that the highest E_g could not be higher than 175 Wh kg^{-1} even if reaching the theoretical capacity 1,675 mAh g^{-1}

Supplementary Table.1 The parameters for predicting E_g

S$_8$ loading (mg cm^{-2})	Electrolyte (mg cm^{-2})	Cathode (mg cm^{-2})	Anode (mg cm^{-2})	Current collector+ separator (mg cm^{-2})	E_g (Wh kg^{-1})
2	**36**	3.1	$0.0016x$	3.4	$\dfrac{4.2x}{42.5 + 0.0016x}$
5	**90**	7.7	$0.004x$	3.4	$\dfrac{10.5x}{101.1 + 0.0016x}$
8	**144**	12.3	$0.0064x$	3.4	$\dfrac{16.8x}{159.7 + 0.0016x}$

*Assuming specific capacity=x mAh g^{-1}, S$_8$ content=65%, E/AM ratio=15 µl mg^{-1}, 2× Li excess, average voltage=2.1 V
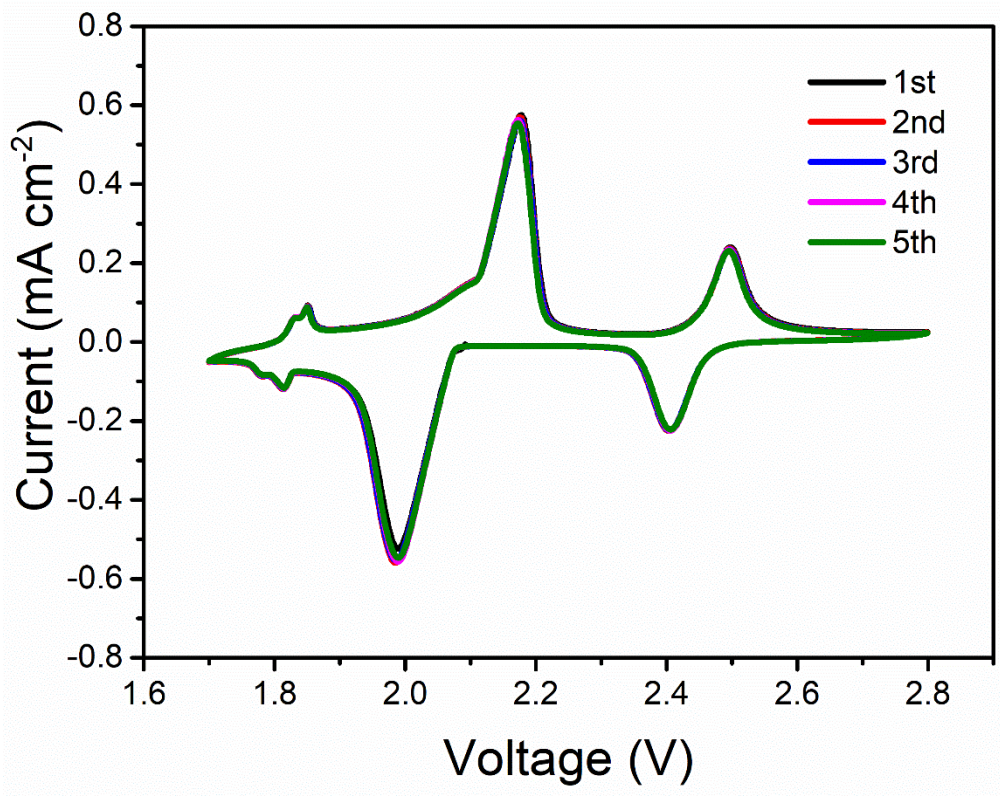
Supplementary Figure 2. The 1st-5th CV profiles of the Mo_6S_8 in the ether-based electrolyte.
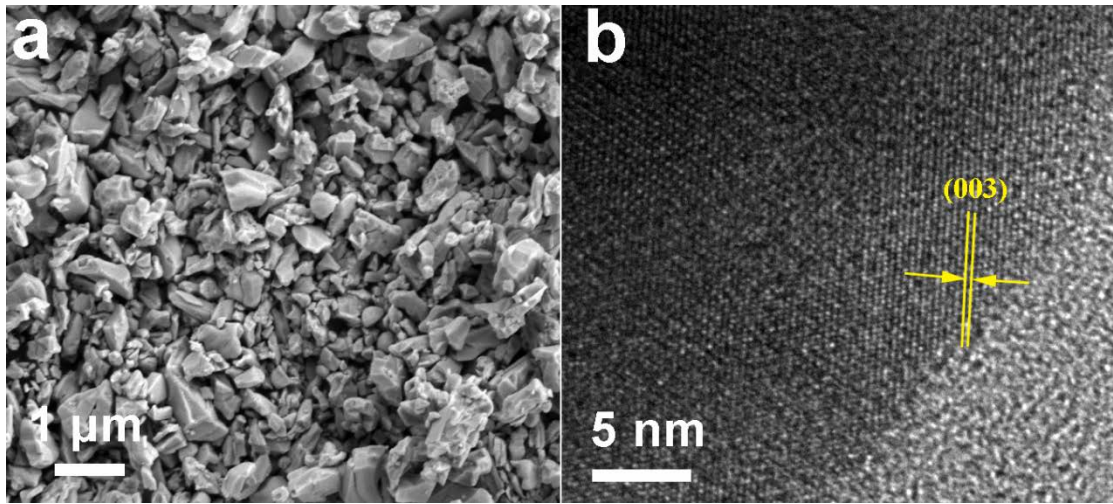
Supplementary Figure 3. Microstructures of the as-prepared Mo_6S_8 powder (a) SEM, (b) HRTEM.
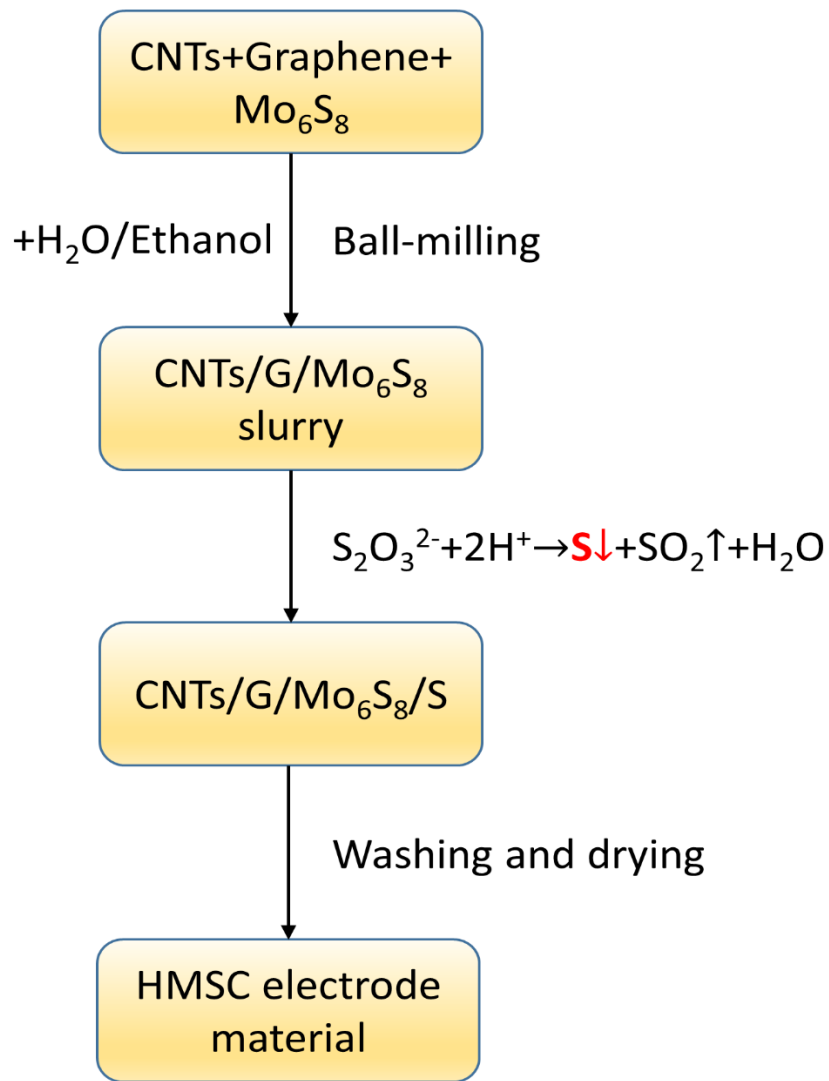
Supplementary Figure 4. The fabrication process of the HMSC material
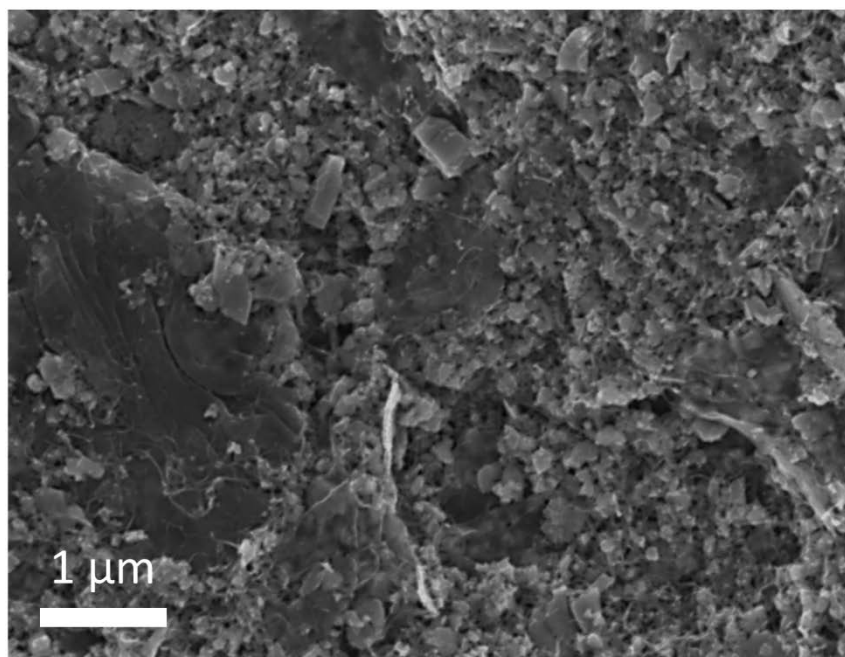
Supplementary Figure 5. SEM image of the CNTs/G/Mo$_6$S$_8$ mixture after ball milling
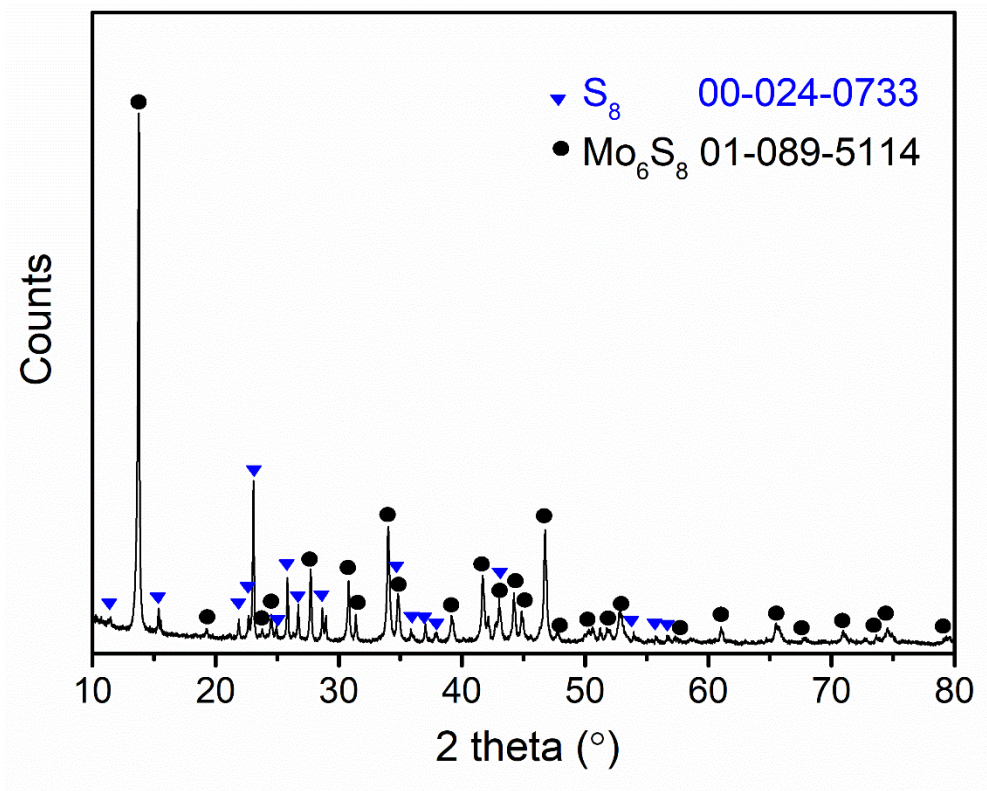
Supplementary Figure 6. XRD pattern of the HMSC material
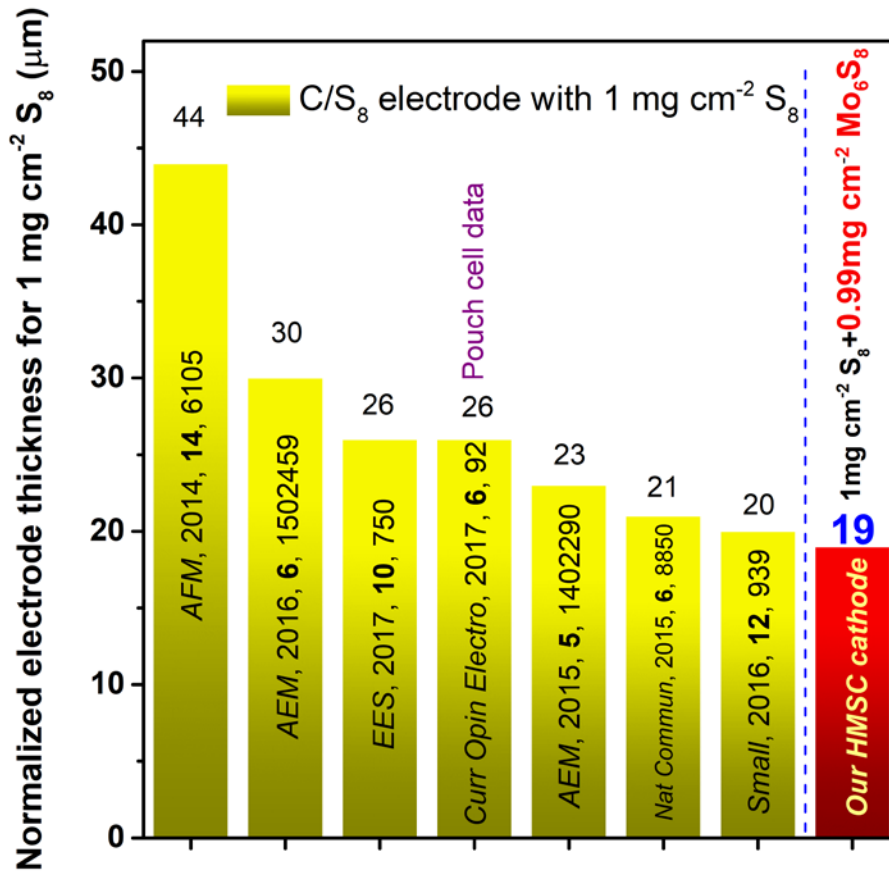
Supplementary Figure 7. Normalized electrode thickness (NET) per 1 mg·cm^{-2} sulfur loading of the HMSC and traditional C/S$_8$ cathodes

The packing density of active materials can be calculated as bellow:
For 19 µm thick electrode containing 1 mg cm^{-2} S$_8$ and 0.99 mg cm^{-2} Mo$_6$S$_8$:

$$S_8: \frac{1\ mg\ cm^{-2}}{19\ \mu m} = 526\ g\ L^{-1}$$

$$Mo_6S_8: \frac{0.99\ mg\ cm^{-2}}{19\ \mu m} = 521\ g\ L^{-1}$$
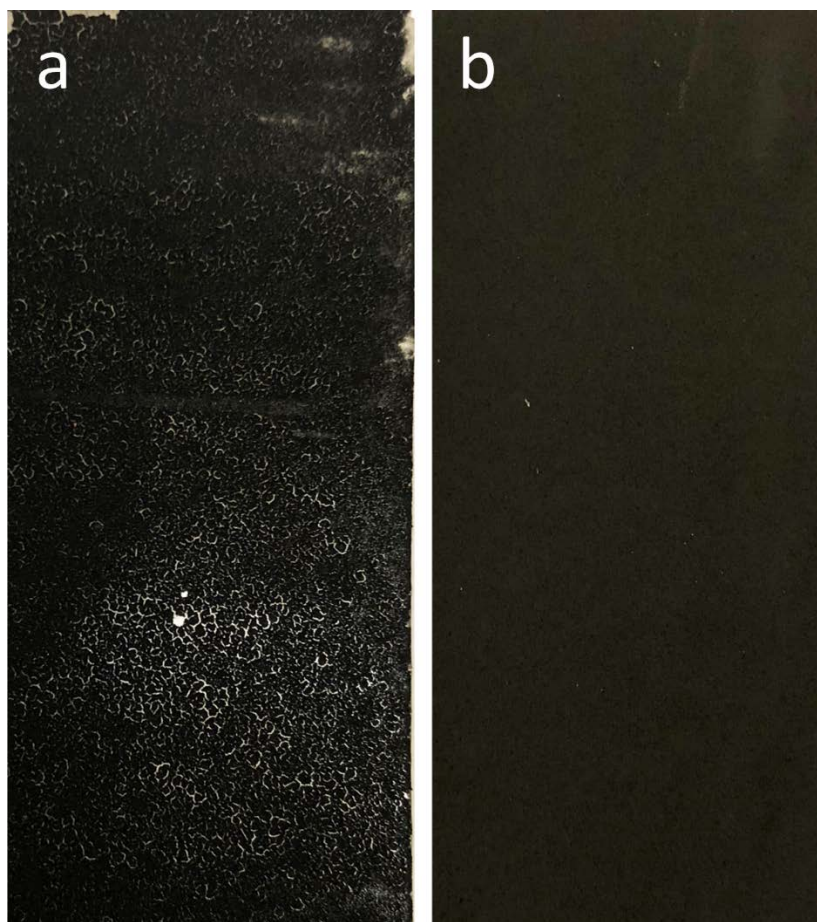
Supplementary Figure 8. Photographs of slurry coating on carbon-coated Al foil with _36% C_/54% S_8 slurry (a) and _10% C_/42.3% Mo_6S_8/42.8% S_8 slurry (b)
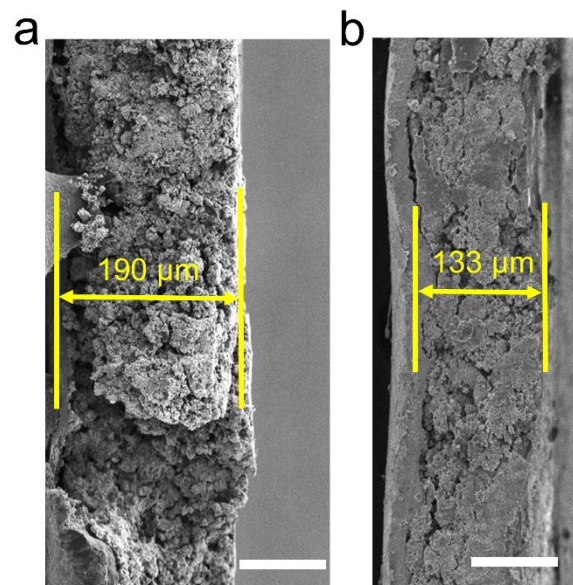
Supplementary Figure 9. SEM figures showing the electrode thickness of cathodes with 10 mg cm^{-2} S$_8$+9.9 mg cm^{-2} Mo$_6$S$_8$ (a) and 6.9 mg cm^{-2} S$_8$+6.8 mg cm^{-2}(b), scale bars 100 µm
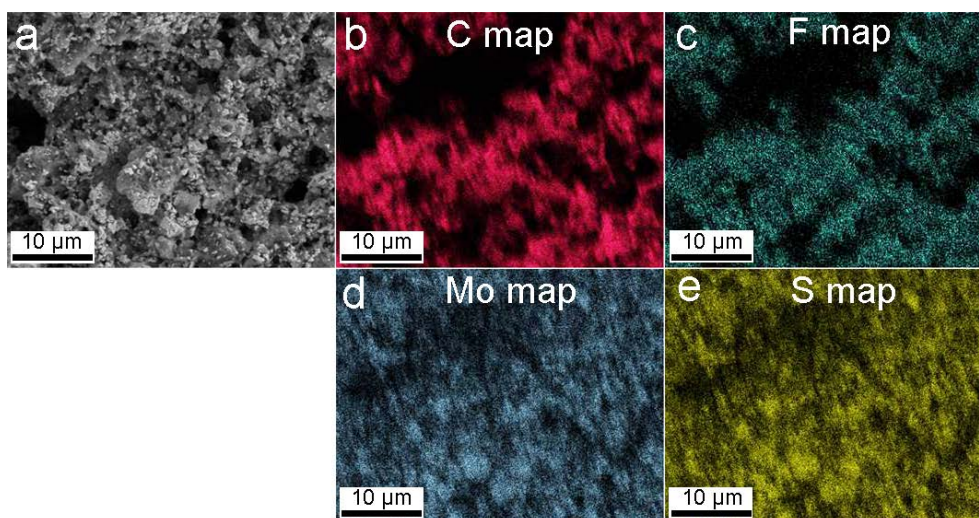
Supplementary Figure 10. The elemental distribution of the cycled HMSC. (a) SEM figure; (b)~(e) EDS mapping of C, F, Mo and S, respectively
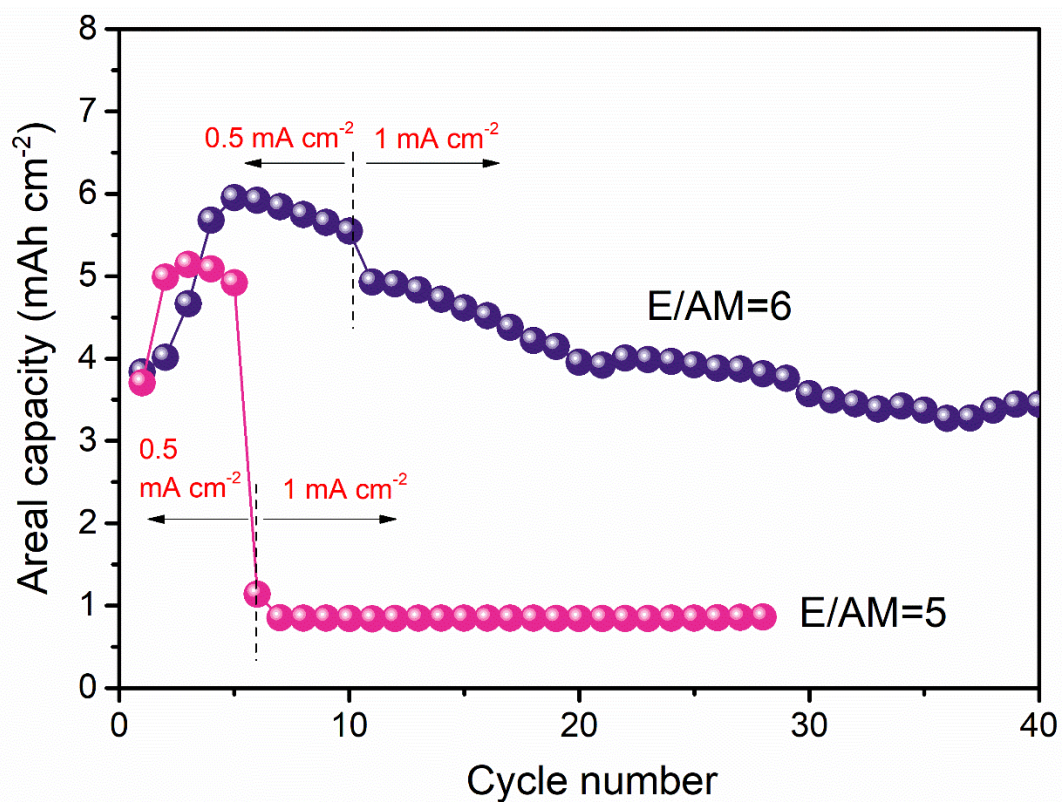
Supplementary Figure 11. Cycling performance of the C/S$_8$ cathode (70 wt% S$_8$+20 wt% C+10 wt% binder, sulfur loading ~5.8 mg cm^{-2}) with different E/AM ratios (μl mg^{-1})
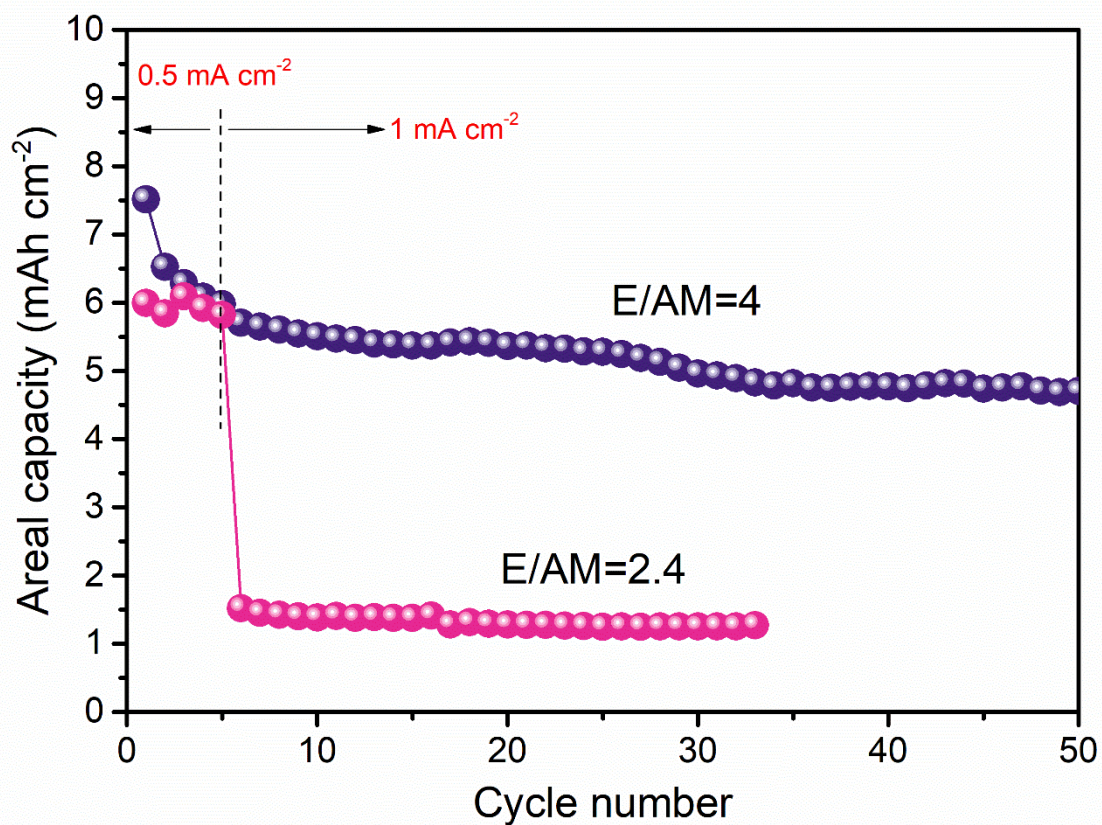
Supplementary Figure 12. Cycling performance of the C/S$_8$/Mo$_6$S$_8$ cathode (65 wt% S$_8$+20 wt% Mo$_6$S$_8$+10 wt% C+5 wt% binder, sulfur loading ~6.0 mg cm^{-2}) with different E/AM ratios (µl mg^{-1})
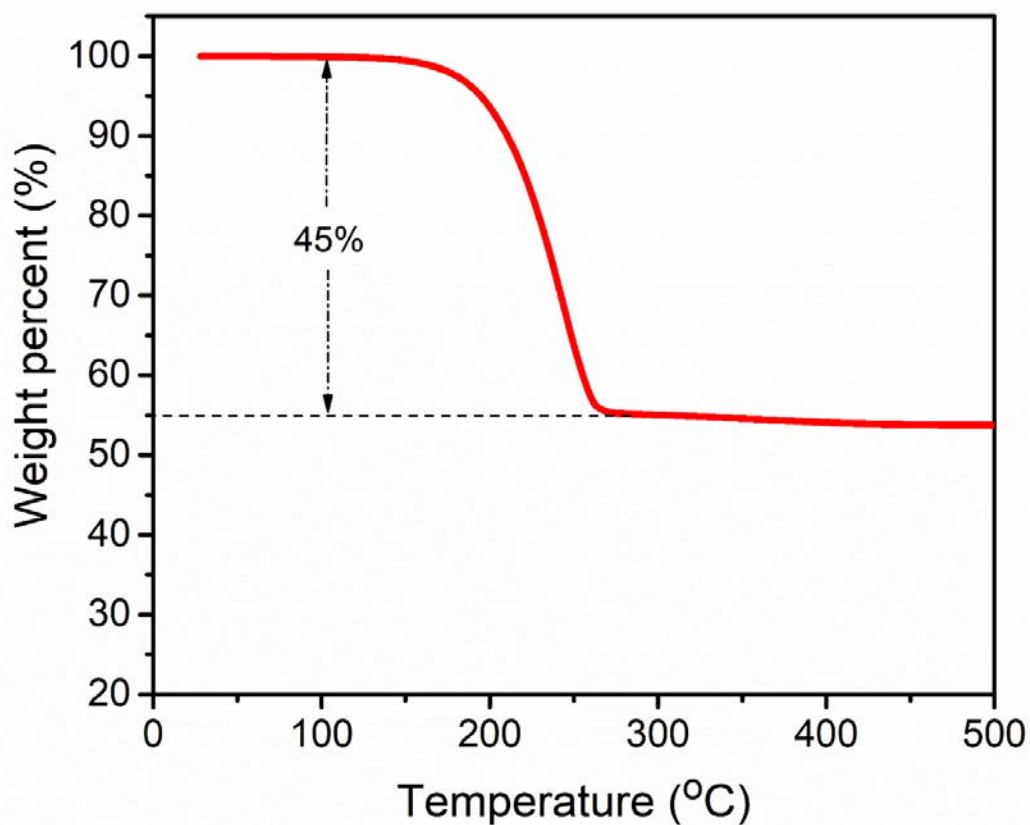
Supplementary Figure 13. Thermogravimetric analysis (TGA) of the HMSC material from room temperature to 500 ℃ at a heating rate of 10℃/min under N_2 atmosphere to determine the sulfur content. 45% sulfur content in HMSC material corresponds to 42.75 % (45%*0.95=42.75%, 95% HMSC material and 5% binder) sulfur content in cathode. So the HMSC consists of 42.25% Mo_6S_8, 42.75% S_8, 10% C and 5% binder).
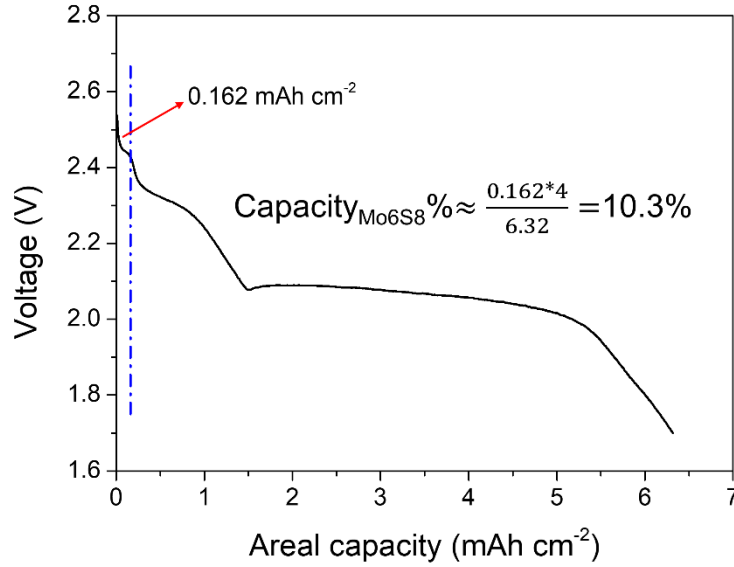
Supplementary Figure 14. The estimation of the capacity contribution from Mo_6S_8

Since the 2nd and 3rd discharging plateaus of Mo_6S_8 are merged with those of S_8, it is difficult to exactly separate the capacity contribution from both active materials. But we can estimate its capacity contribution as following.

As we discussed in the main text, within the operating voltage window of Li-S batteries from 1.7 V to 2.8 V, the stoichiometry of Li insertion into Mo_6S_8 involves three stages. The capacity of Mo_6S_8 could be ~4 times of the capacity contributed by the 1st discharging plateau. The areal capacity from the 1st plateau is ~0.162 mAh cm^{-2}. So the capacity contribution from Mo_6S_8 can be estimated by,
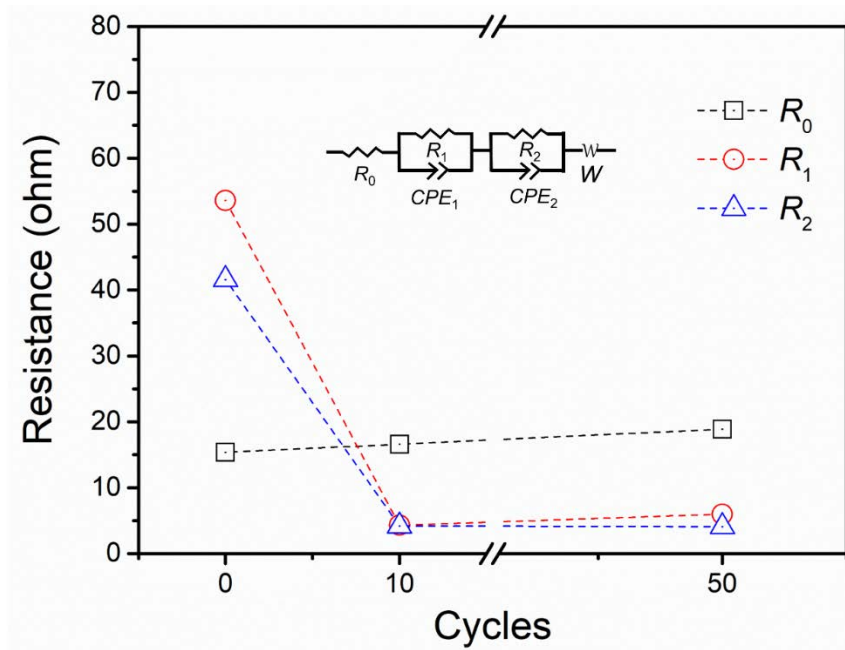
$$\text{Capacity}_{Mo6S8}\% \approx \frac{0.162 \ mAh \ cm^{-2}*4}{6.32 \ mAh \ cm^{-2}} = 10.3\%$$
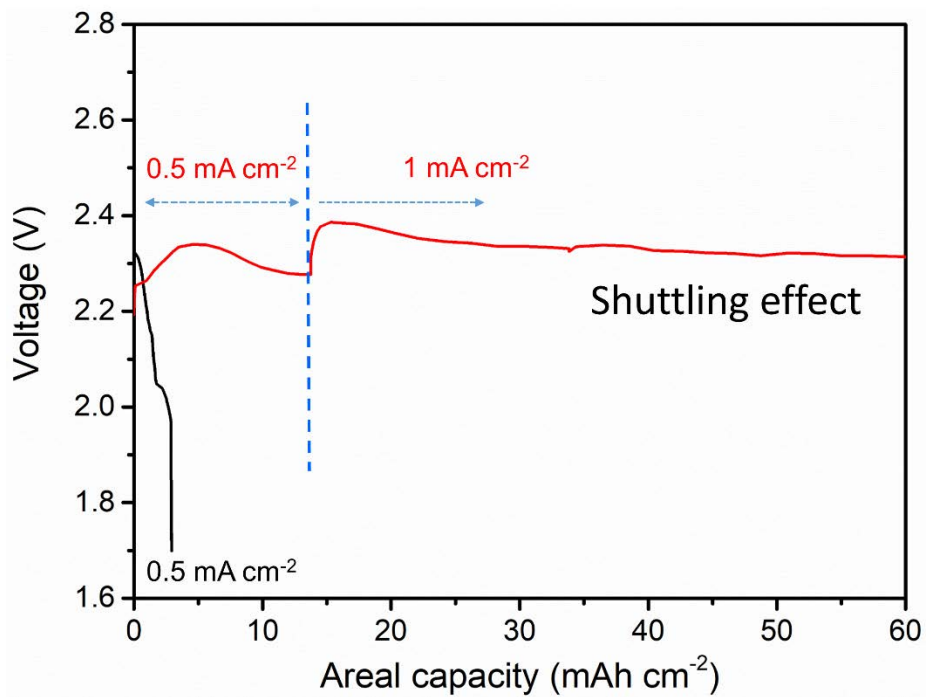
Supplementary Figure 15. The obvious shuttling effect of the C/S_8 cathode without Mo_6S_8 (85 wt% S_8+10 wt% C+5 wt% binder, sulfur loading ~6.5 mg cm^{-2}, E/AM ratio ~2.4 µl mg^{-1})
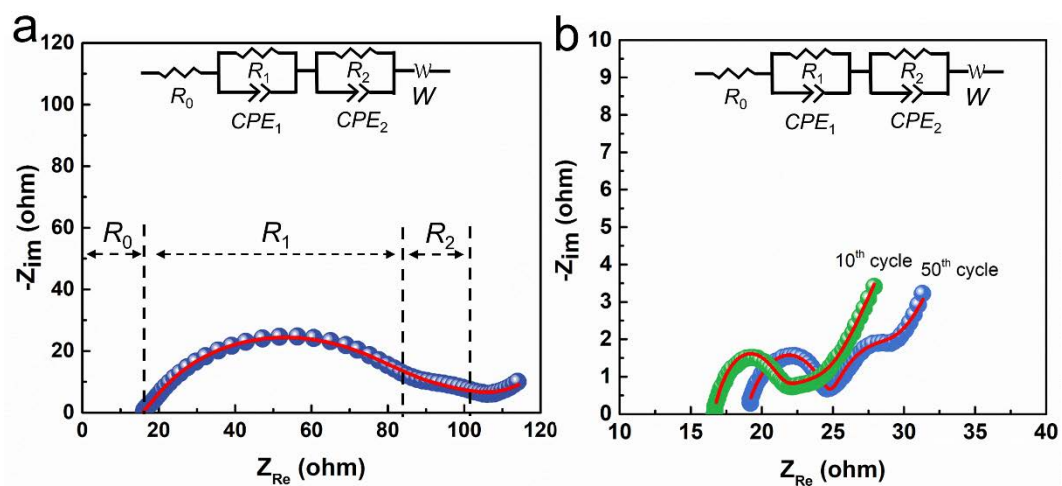
Supplementary Figure 16. EIS analysis of the Li|HMSC cell before (a) and after cycling (b) for 10 and 50 cycles.

Supplementary Figure 17. Fitting parameters of EIS plots in Supplementary Fig. 16 before cycling and after 10 and 50 cycles.
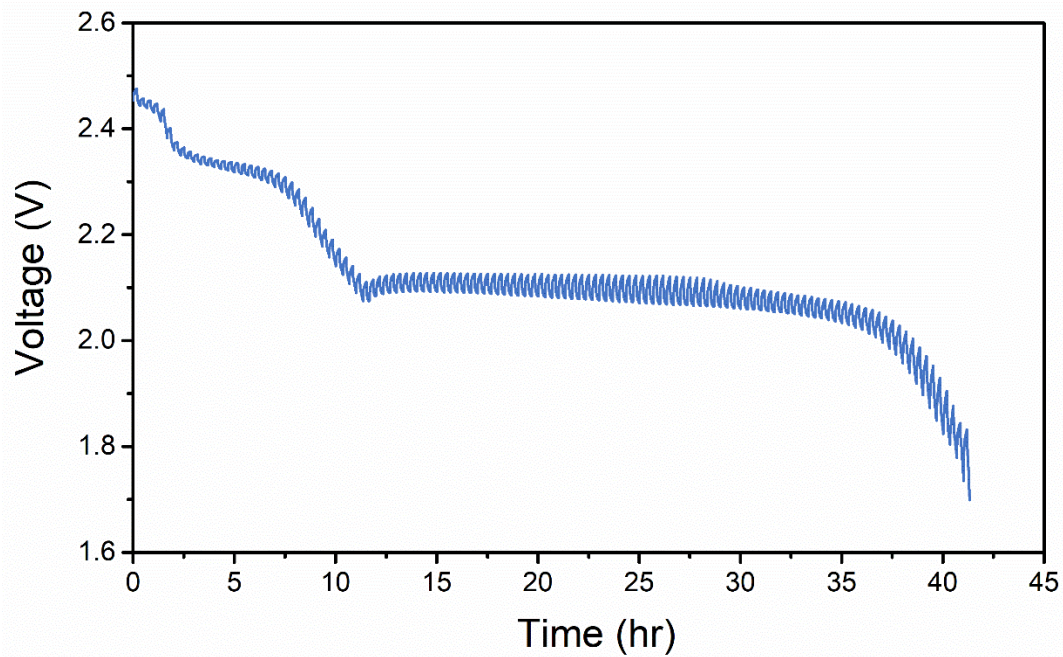
Supplementary Figure 18. Galvanostatic intermittent titration technique (GITT) curve vs. time with a discharging current density of 0.25 mA cm^{-2} using the cell after cycling for 100 cycles
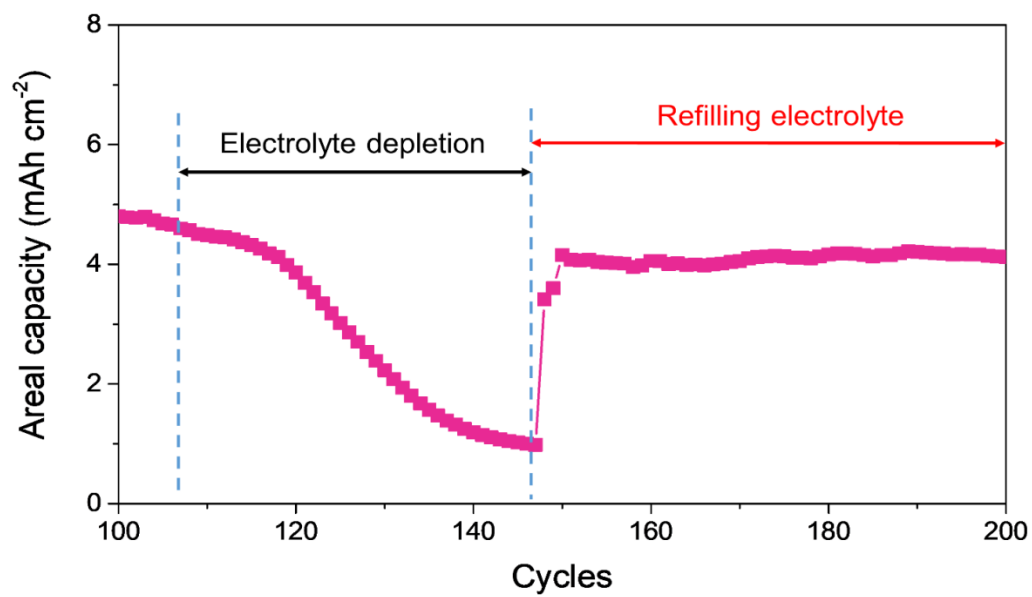
Supplementary Figure 19. Cycling performance after 100 cycles and refilling electrolyte in Fig. 5c in the main text
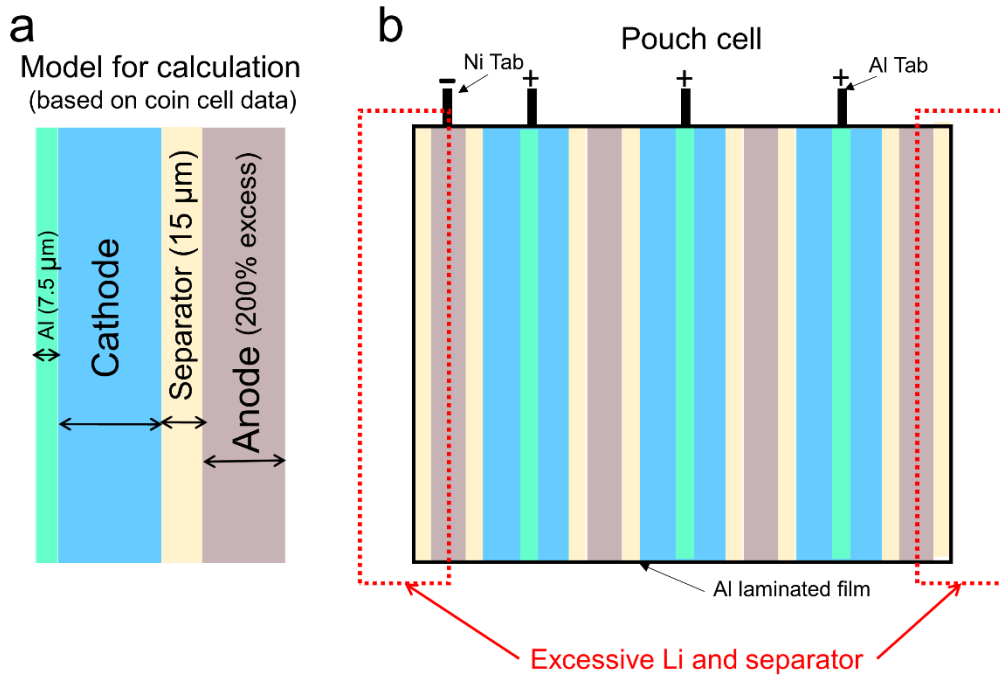
Supplementary Figure 20. The difference between the ideal and actual pouch cell configurations. (a) The simplified configuration for calculating coin cell data; (b) The actual pouch cell configuration

The slight difference between the energy densities estimated by theoretical model and the actual pouch cell is mainly due to following reasons. First, the difficulty in maintaining the high quality of the HMSC material when transferring to mass production requiring long-term optimization of various parameters. We believe that there will be a great improvement in electrochemical performances after this optimization. Second, there are more components in the real pouch cell (b) than the simplified model (a). In addition, the thickness of the separator is 15 μm in model but 25 μm in the pouch cell.
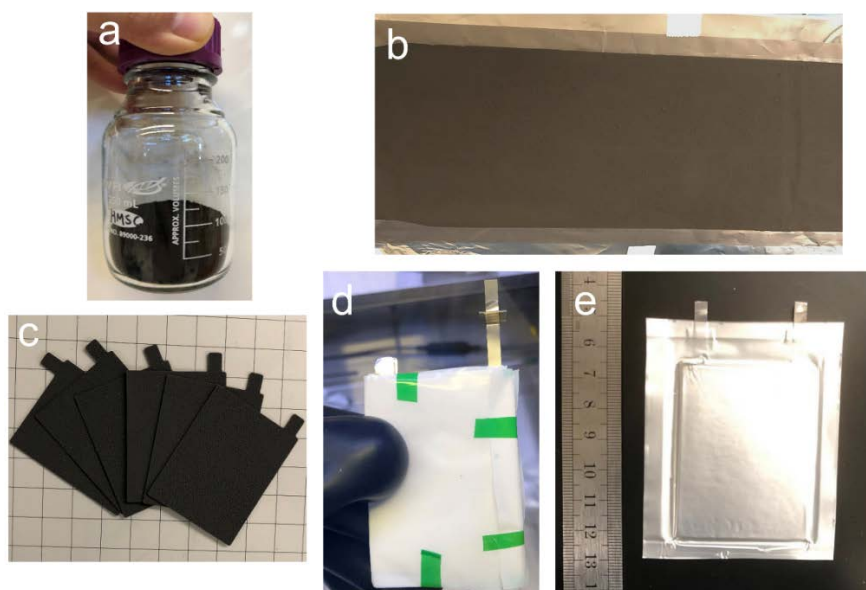
Supplementary Figure 21. The whole process to make Li-HMSC pouch cell
(a) Mass production of the HMSC material; (b) The electrode after double-side coating and drying; (c) Electrodes cut by a gas driven die cutter; (d) The jellyroll cell after hand-stacking; (e) The pouch cell after injecting electrolyte and vacuum-sealing.
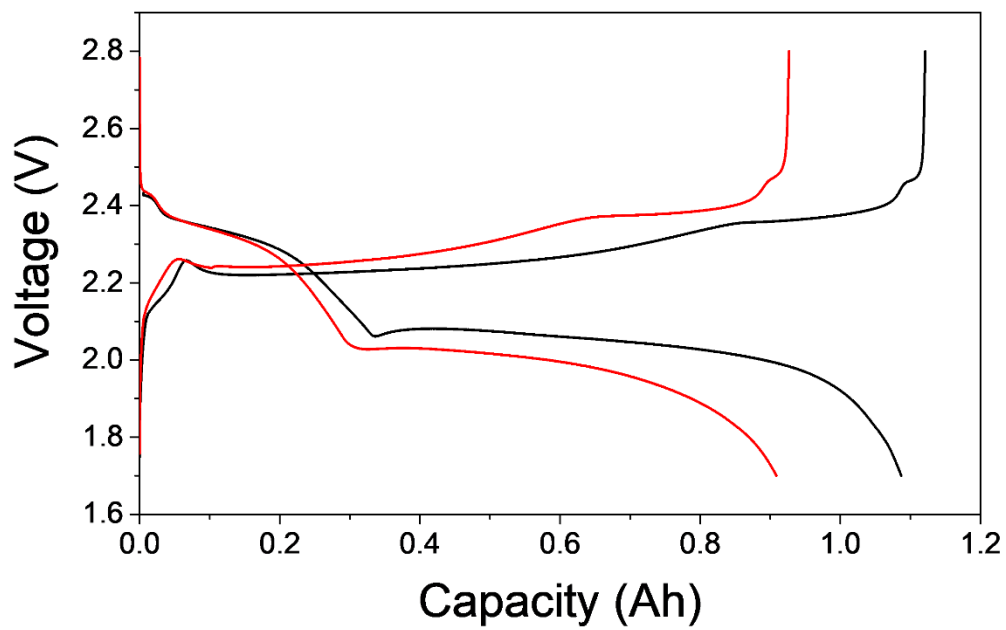
Supplementary Figure 22. The voltage profiles of the Li|HMSC pouch cell with E/AM ratio low to 1.2 μL mg^{-1} and 2× Li excess
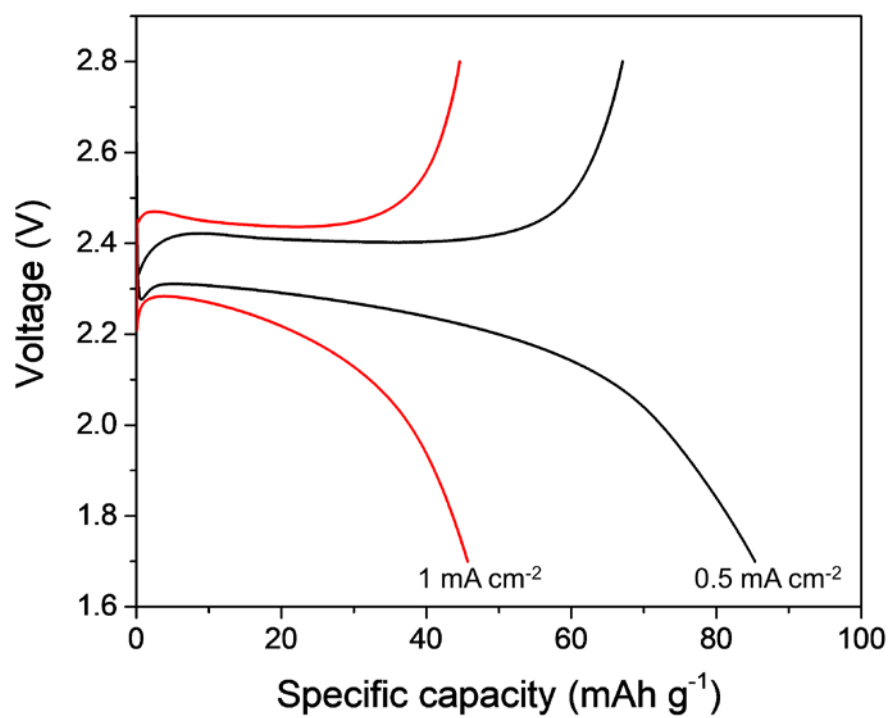
Supplementary Figure 23. The electrochemical property of the Li-S pouch cell with 3 layers of double-side coated C/S_8 cathodes with an E/AM ratio of 1.3 µl mg^{-1}.
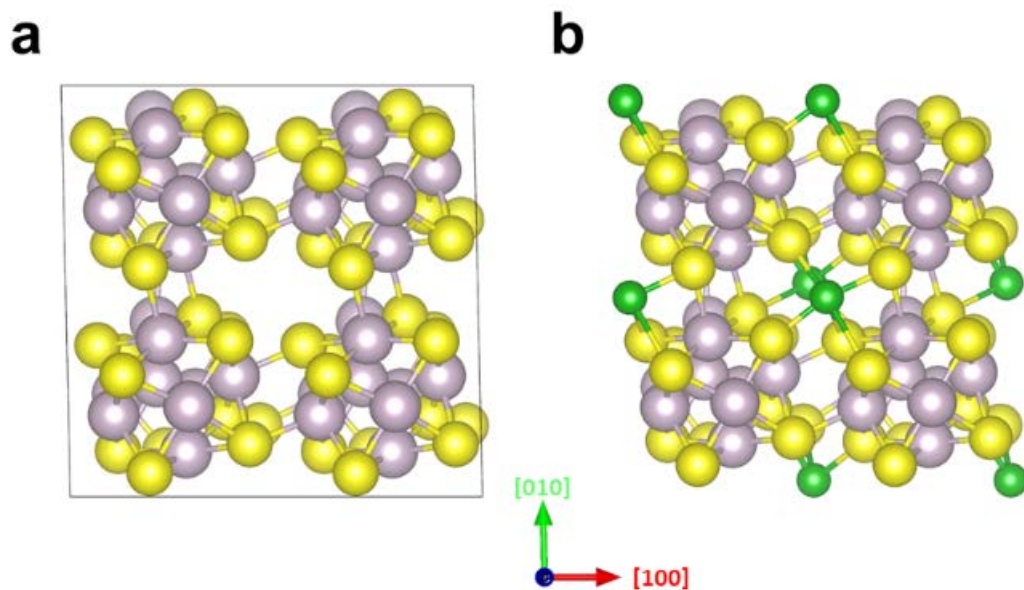
Supplementary Figure 24. Optimized geometry of the configuration of (a) pristine Mo_6S_8 and (b) Li-intercalated Mo_6S_8 ($LiMo_6S_8$).
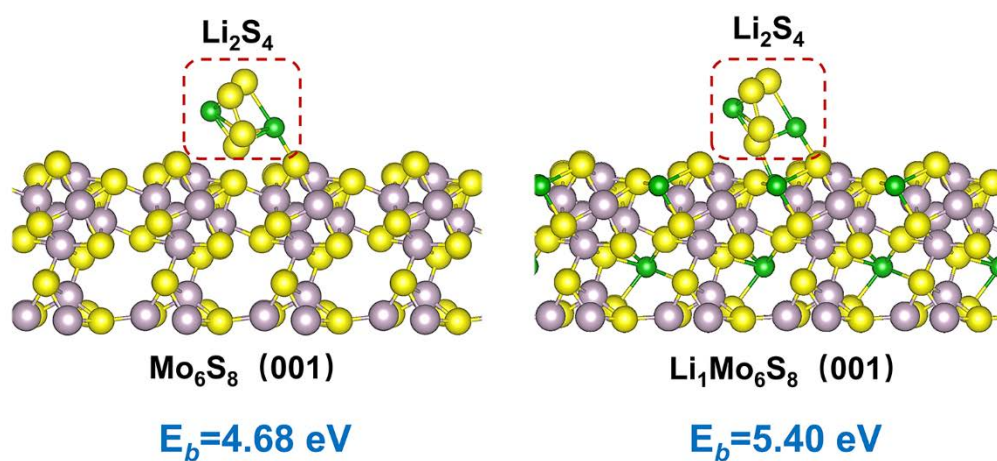
Supplementary Figure 25. Relaxed structure of Li_2S_4 (without ionization) absorbed upon (100) in Mo_6S_8 and $LiMo_6S_8$.

Supplementary Notes

Supplementary Note 1 Theoretical prediction of the relationship between energy densities and cathode porosity

For theoretical prediction of the relationship between energy densities and cathode porosity (Fig. 1 in main text), we correlate the required electrolyte amount to porosity by assuming that the electrolyte fills all the porosity in cathode. The cathode is assumed to consist of pure S_8 or Mo_6S_8/S_8 (3:7 and 5:5 by weight) or C/S_8 (3:7 and 5:5 by weight) without any additives. We use the theoretical energy densities of sulfur (1672 mAh g^{-1}×2.1 V=3511 Wh kg^{-1}) and Mo_6S_8 (128 mAh g^{-1}×2.1 V=269 Wh kg^{-1}) for calculation with the assumption that there is a (g) solid in cathode and the cathode porosity is $x\%$. m, V and ρ are the mass, volume and density of materials appearing as subscripts.

The electrolyte mass can be calculated as bellow,

$$m_{electrolyte} = V_{porosity} \cdot \rho_{electrolyte}$$

$$= V_{solid} \cdot \frac{x\%}{1-x\%} \cdot \rho_{electrolyte}$$

$$= \sum \frac{m_{solid}}{\rho_{solid}} \cdot \frac{x\%}{1-x\%} \cdot \rho_{electrolyte} \tag{1}$$

The total energy delivered by electrochemically-active materials can be calculated

$$E = \sum m_{active} \cdot E_{active} \tag{2}$$

So the E_g of cathode and electrolyte can be calculated

$$E_g = \frac{E}{m_{solid} + m_{electrolyte}}$$

$$= \frac{E}{a + m_{electrolyte}} \tag{3}$$

The E_v of cathode and electrolyte can be calculated

$$E_v = \frac{E}{V_{solid}/(1-x\%)} \tag{4}$$

Supplementary Table. 2 The volume of solid materials

Materials	Pure S_8	Mo_6S_8:S_8=3:7	Mo_6S_8:S_8=5:5	C:S_8=3:7	C:S_8=5:5
V_{solid} (cm^{-3})	$\dfrac{a}{2.07}$	$\dfrac{0.3a}{5.04}+\dfrac{0.7a}{2.07}$	$\dfrac{0.5a}{5.04}+\dfrac{0.5a}{2.07}$	$\dfrac{0.3a}{2.02}+\dfrac{0.7a}{2.07}$	$\dfrac{0.3a}{2.02}+\dfrac{0.7a}{2.07}$

Supplementary Table. 3 The energy delivered by electrochemically-active materials

Materials	Pure S_8	Mo_6S_8:S_8=3:7	Mo_6S_8:S_8=5:5	C:S_8=3:7	C:S_8=5:5
E (mWh)	$3511a$	$(0.3 \times 269 + 0.7 \times 3511)a$	$(0.5 \times 269 + 0.5 \times 3511)a$	$0.7 \times 3511a$	$0.5 \times 3511a$